

Nature of the Structural Symmetries Associated with Hybrid Improper Ferroelectricity in $\text{Ca}_3\text{X}_2\text{O}_7$

S. Liu¹, H. Zhang¹, S. Ghose^{2,*}, M. Balasubramanian³, Zhenxian Liu⁴, S. G. Wang⁵, Y-S. Chen⁵, B. Gao^{6,7}, J. Kim^{6,7}, S.-W. Cheong^{6,7}, B. Nowadnick^{1,7}, and T. A. Tyson^{1,7,*}

¹Department of Physics, New Jersey Institute of Technology, Newark, NJ 07102

²National Synchrotron Light Source II, Brookhaven National Laboratory, Upton, NY 11973

³Advanced Photon Source, Argonne National Laboratory, Argonne, IL 60439

⁴Institute of Materials Science, Department of Civil and Environmental Engineering, The George Washington University, Washington, DC 20052

⁵Center for Advanced Radiation Sources, University of Chicago, Argonne, IL 60439

⁶Department of Physics and Astronomy, Rutgers University, Piscataway, NJ 08854

⁷Rutgers Center for Emergent Materials, Rutgers University, Piscataway, NJ 08854

*Corresponding Authors: T. A. Tyson, e-mail: tyson@njit.edu
S. Ghose, e-mail: sghose@bnl.gov

Abstract

In hybrid improper ferroelectric systems, polarization arises from the onset of successive nonpolar lattice modes. In this work, measurements and modeling were performed to determine the spatial symmetries of the phases involved in the transitions to these modes. Structural and optical measurements reveal that the tilt and rotation distortions of the MnO_6 or TiO_6 polyhedra relative to the high symmetry phases driving ferroelectricity in the hybrid improper $\text{Ca}_3\text{X}_2\text{O}_7$ system ($X=\text{Mn}$ and Ti) condense at different temperatures. The tilt angle vanishes abruptly at $T_T \sim 400$ K for $\text{Ca}_3\text{Mn}_2\text{O}_7$ (and continuously for $X=\text{Ti}$) and the rotation mode amplitude is suppressed at much higher temperatures $T_R \sim 1060$ K. Moreover, Raman measurements in $\text{Ca}_3\text{Mn}_2\text{O}_7$ under isotropic pressure reveal that the polyhedral tilts can be suppressed by very low pressures (between 1.4 and 2.3 GPa) indicating their softness. These results indicate that the $\text{Ca}_3\text{Mn}_2\text{O}_7$ system provides a new platform for strain engineering of ferroelectric properties in film based systems with substrate induced strain.

I. Introduction

A broad range of mechanisms are known to produce ferroelectricity in solid materials including intrinsically atomic effects such as the lone pairs (e.g. $6s^2$ in BiFeO_3 [1]) or ion size mismatch leading to off-center lattice distortions in the classical BaTiO_3 system [2]. From a microscopic perspective, these materials fall into two main classes having net electric polarization due to atomic displacement, such as the ABO_3 system, where an off-center B atom displacement is proposed. Alternatively, order-disorder transitions have also been proposed in these systems. In general, the microscopic mechanisms driving ferroelectric behavior are thought to cause a gamma point instability in the ordering of a polar mode of the parent structure. There is a direct connection between the polarization amplitude and the structural polar mode.

Distinct from these mechanisms above are a class of improper ferroelectrics in which the polarization is a secondary order parameter. Recently, the layered perovskites ($n=2$ Ruddelsen-Popper structure with double stacked MnO_6 polyhedra, $\text{A}_3\text{B}_2\text{O}_7$) was predicted to support ferroelectric induced by the introduction of a rotation pattern due to two independent nonpolar rotations of the BO_6 polyhedra [3] relative to the high symmetry $I4/mmm$ (#139) phase at high temperature. The structure is characterized by an X_2^+ rotation of the MnO_6 polyhedra in the high symmetry plane and a X_3^- tilt relative to the high symmetry (long) axis. The polarized state of this system is determined by the combined rotation and tilt structural modes. In these hybrid improper ferroelectrics, DFT calculations reveal that the symmetry of the phase exhibiting ferroelectricity has space group $A2_1am$ (#36, $\text{Cmc}2_1$ in standard setting). The rotations couple directly with the magnetic order of the Mn sites (having G type antiferromagnetic order) at low temperature [4].

The nature of the transition from the high-temperature $I4/mmm$ phase to the low-temperature $A2_1am$ phase is not well understood. Determination of whether the rotation and tilt structural changes onset collectively or separately, the nature of the transitions (first or second order), and the appropriate long range and local symmetries present is essential to the development of accurate theoretical models.

Limited structural powder diffraction work suggests that the $\text{Ca}_3\text{Mn}_2\text{O}_7$ system undergoes a transition into an intermediate Acaa phase (#68, Ccca standard setting) [5]. In polycrystalline samples, the proximity of the Acaa and $\text{A2}_1\text{am}$ phase in energy was found to produce a broad mixed phase region. Additional symmetry possibilities of the intermediate state include the Acam, Amam and F2mm space groups. While clear switchable ferroelectric polarization has been observed in Ti and Sn-based systems (B site), the manganese perovskite system has not been seen to exhibit this critical behavior needed for device applications. A complex domain structure with the stacking of a and b domains along the c axis (long axis) has been found to suppress polarization in $\text{Ca}_3\text{Mn}_2\text{O}_7$ [6]. The primary difference between $\text{Ca}_3\text{Mn}_2\text{O}_7$ (with the coupling of magnetic order and structure but no finite electric polarization) and the $\text{Ca}_3\text{Ti}_2\text{O}_7$ (with large electric polarization, $8 \mu\text{C}/\text{cm}^2$) [7] is the stability of $\text{A2}_1\text{am}$ low-temperature phase in the Ti-based system over a broad range of temperatures and its switchable room temperature electric polarization.

Systematic studies of the $\text{Ca}_3\text{Mn}_{2-x}\text{Ti}_x\text{O}_7$ mixed system have been initiated to understand the electric polarization domain structure and magnetic order in this system [5]. Recent Raman measurements up to 350 K on single crystals of $\text{Ca}_3\text{Mn}_2\text{O}_7$ indicate a significant softening of a mode near 107 cm^{-1} which was assigned to be an antiphase tilting mode based on phonon calculations utilizing classical interaction potentials [8]. Shifts in the modes corresponding to tilting and rotation were examined, and it is argued that reduction of the frequency of the tilting mode with temperature indicates that this is a transition from Cmc2_1 ($\text{A2}_1\text{am}$) to an assumed Ccca (Acaa) intermediate phase is driven by a tilt rotation. An intermediate phase region with the coexistence of competing soft modes with distinct phases was found to be consistent with these measurements. However, no direct structural information was presented.

Neutron diffraction and laboratory based x-ray diffraction structural measurements on the B site (Ti or Mn) doped system $\text{Ca}_3\text{Mn}_{0.9}\text{Ti}_{0.1}\text{O}_7$ found antiphase tilting of the MnO_6 polyhedra decreases in amplitude while the rotation remains unchanged with increasing temperature and pressure [9]. The tilting was found to decrease smoothly (from $\sim 8^\circ$ to $\sim 6.5^\circ$), going from $\sim 10 \text{ K}$ to $\sim 375 \text{ K}$, with a kink near the

magnetic ordering temperature T_N . In the analysis in that work, the single-crystal neutron scattering measurements reveal a polar $Aba2$ space group at 450 K. It was indicated that $Ca_3Ti_2O_7$, by contrast, would have enhancement of both antiphase tilt and in-plane distortion with increasing temperature.

To fully understand the nature of the transitions in this material, structural measurements on the endmember $Ca_3Mn_2O_7$ and $Ca_{2.4}Sr_{0.6}Ti_2O_7$ (representing $CaTiO_3$) were conducted over a broad temperature range. Samples derived from single crystals were used in all measurements. Heat capacity (2 K to 380 K) and differential scanning calorimetry (DSC, 300 K to 500 K) measurements were conducted. Local structural pair distribution function (PDF) measurements were conducted between 100, and 1100 K at the NSLS II XPD (28ID-2) Beamline and APS beamline 6-ID-D. X-ray absorption (XAFS and XANES) measurements were conducted with respect to the Mn site for the temperature range 300 K and 1100 K (at beamline 8-ID at NSLS II), and with respect the Ca site (at APS beamline 20 BM- for temperatures near the ~ 400 K transition). High-resolution synchrotron single crystal diffraction measurements were conducted between 100 K and 480 K (at APS beamline 15-ID-D). High-pressure Raman measurements were conducted at NSLS2 beamline 22-IR-1 to follow the changes in symmetry with pressure and determine the pressure ranges for the phase changes. Experimental and computation details are provided in the Supplementary Document.

Calorimetry measurements (differential scanning calorimetry (DSC) and heat capacity) reveal a second order transition near 110 K corresponding to the antiferromagnetic ordering temperature and a first-order transition near 367 K on cooling and near 405 K on warming in $Ca_3Mn_2O_7$. This first order transition is found in structural measurements corresponding to a loss of tilt angle (vanishing of X_3^- tilt amplitude) above this transition on warming and yields a nonpolar space group ($I4/mmm$ or $C2/m$ with split in-plane oxygen sites). The transition temperature is termed T_T . Distinct domains with the same space group are found. These measurements are supported by Raman observations. Local structural measurements reveal enhanced Ca-Mn bond order on warming above T_T consistent with loss of electric polarization. No evidence of phase coexistence is found near T_T . In this temperature region, thermal

measurements reveal no clear phase transitions in polycrystalline samples. PDF and XAFS measurements reveal a transition near 1060 K consistent with the loss of the X_2^+ rotation amplitude (termed T_R).

In this work, parallel structural and spectroscopic measurements, conducted on the corresponding Ti-based system $\text{Ca}_{3-x}\text{Sr}_x\text{Ti}_2\text{O}_7$ ($\text{Ca}_{2.4}\text{Sr}_{0.6}\text{Ti}_2\text{O}_7$), reveal the same trend. However the loss of the X_3^- tilt amplitude is found to be a continuous transition. DFT calculations on both $\text{Ca}_3\text{Mn}_2\text{O}_7$ and $\text{Ca}_3\text{Ti}_2\text{O}_7$ indicate that the relevant self force constant for the O sites are significantly softer for a local tilt distortion compared to local twist or rotational local distortion, consistent with the measurements. The phonon density of states of both systems are qualitatively similar. The essential overview of the general $\text{Ca}_3\text{X}_2\text{O}_7$ system is that near T_T (~400 K) the tilt mode vanishes, while the rotational mode amplitude decreases continuously with increase temperature. High-pressure Raman measurements indicate loss of tilt angle for very low pressures (between 1.4 and 2.3 GPa) revealing the softness of the tilt mode. Preparing thin film samples with substrate strain values near this critical cross-over value in strain (near ferro/paraelectric transition) will enable switching of polarization (on/off) using a piezoelectric substrate. The results also suggest that enhancement of the A-O bond strength will lift the temperature T_T at which the polarization vanishes. Work on the X=Mn system is presented in the main text and the X=Ti system results are included in the supplementary document.

II. Qualitative Structure, Predicted Phonon Spectra and Raman Measurements

Figure 1(a) shows the crystal structure of $\text{Ca}_3\text{Mn}_2\text{O}_7$ with respect to the $\text{Cmc}2_1$ space group (#36, standard setting) with the long-axis along a. Note that there are three distinct types of O sites in this n=2 Ruddlesden-Popper perovskite system. There are apical O sites bonded only to one Mn site and weakly bonded to the Ca sites, apical interior sites shared by two Mn sites along the a-axis (a-axis, long axis for this space group setting) and planar O sites shared between two Mn sites in the b-c plane. Fig. 1(b) shows

the MnO_6 polyhedral rotation about the long axis (X_2^+ , black curved arrow) and the tilts (X_3^- , blue arrows) of the polyhedra normal to the long axis.

Calculation of the force constants by DFT methods enables computation of the phonon density of states. Fig. 1(c) shows the phonon density of states (DOS) projected onto the Mn, Ca and O sites exclusively. What can be seen is that although the Ca atoms are lower in mass than the Mn atoms, the main peak in the phonon DOS at low energy is primarily from the Ca site. The Mn contributions are broad and extend up to $\sim 500 \text{ cm}^{-1}$ while the O DOS covers the full energy range. Hence Ca atom motions dominate the low-frequency phonon modes while oxygen contributes at all frequencies. The similarity of the force constants indicates similar phonon DOS for $\text{Ca}_3\text{Mn}_2\text{O}_7$ and $\text{Ca}_3\text{Ti}_2\text{O}_7$. Indeed theoretical work on $\text{Ca}_3\text{Ti}_2\text{O}_7$ yield qualitatively similar phonon DOS [10] to that presented in Fig. 1(c).

Raman measurements were conducted on single crystal, and polycrystalline samples for temperatures between 100 and 500 K, covering the high end of any possible low-temperature transitions. In Fig. 2(a) we show spectra for the incident laser beam normal to the long axis (x-axis). Note the abrupt change in frequency in the peak near 615 cm^{-1} on cooling below $\sim 370 \text{ K}$ (breathing mode of MnO_6 polyhedra, see below). Near the same temperature, the peak near 460 cm^{-1} also vanishes. We note that a weak low-frequency peak near 146 cm^{-1} in the spectrum is found to vanish with increasing temperature (see arrow in Fig. 2(a)). The area of this peak vs. temperature is given in Fig. 2(b) indicates the abrupt drop-off with temperature. For the same measurement geometry, the peak position of the main peak near 615 cm^{-1} is shown on warming and cooling in Fig 2(c) and in Fig. S4(b). The abrupt transition is characteristic of first-order behavior. Measurement of a polycrystalline sample over the same temperature range reveals no step change, consistent with earlier measurements [4] on the same type of material suggesting mixed phase behavior. Fig. S1 (supplementary document) shows the calculated displacement modes from DFT for phonons near 129 cm^{-1} and 142 cm^{-1} (Fig. S1(a), Fig. S1(b) and Table S1.). The lowest energy mode (129 cm^{-1}) corresponds to the shear motion of the Ca ion near the apical O atoms. While the calculated mode at 142 cm^{-1} corresponds to the combined planar motion of the Ca sites and tilt rotations of the MnO_6 polyhedra. For both modes, all Ca atomic motions are in the yz plane containing

the electric polarization vector. The main peak at 612 cm^{-1} (Fig. S1(c)) is characterized by a breathing mode of the MnO_6 polyhedra. The full set of calculated phonon-frequencies at the gamma point are given in Table S1. The corresponding Raman spectra in a offset configuration for the laser beam normal to and along the long axis are given in Fig. S2. The measurements for the beam along the symmetry axis show suppression of the peak near 120 cm^{-1} with increasing temperature (Fig S3, and additional surface plots in Fig S4).

III. Calorimetric Measurements

Heat capacity and DSC measurements on crystals of $\text{Ca}_3\text{Mn}_2\text{O}_7$ were used to identify the nature of the observed transitions. Low-temperature heat capacity measurements (Fig. S5) on both warming and cooling reveal a smooth transition near 110 K corresponding to the magnetic ordering temperature (T_N). The absence of hysteresis and the step-like shape indicates that the transition is second order. DSC measurements on crystals of at higher temperature (Fig. 3) reveal an abrupt structural transition at 405 K on warming and at 367 K on cooling the sample, indicating that the transition is first order in nature. No transition features are seen in the corresponding polycrystalline sample measurements (derived from solid state reaction, Fig.S6(a)).

DSC measurements for $\text{Ca}_{2.4}\text{Sr}_{0.6}\text{Ti}_2\text{O}_7$ indicate a very weak feature with the characteristic step change observed for continuous or glass-like transitions (Fig. S6(b)). Raman measurements on single crystal $\text{Ca}_{2.4}\text{Sr}_{0.6}\text{Ti}_2\text{O}_7$ (stabilized by Sr doping) between 100 and 500 K (Figs. S7 and S8) indicate low-frequency phonons near 93 and 112 cm^{-1} soften smoothly with temperature indicating a continuous transition. Similar behavior is seen in polycrystalline samples of $\text{Ca}_3\text{Ti}_2\text{O}_7$ with low-frequency phonons near 121 cm^{-1} (Figs. S9 and S10). The combined results indicate that the transition at T_T is first order for the $X=\text{Mn}$ system and continuous for the $X=\text{Ti}$ system.

IV. Local Structural Measurements (X-Ray Absorption Spectroscopy)

Detailed structural measurements on $\text{Ca}_3\text{Mn}_2\text{O}_7$ were conducted to determine the changes in local and long-range structure with temperature. XAFS measurements relative to the Mn site were used to determine the changes in local structure between 300 and 1100 K (Fig. 4). Fits were made for Mn-O, Mn-Ca and Mn-Mn bond (covering the range up to $\sim 4 \text{ \AA}$, Fig S11). At high temperatures (Fig. 5(a) and 5(b)) the Mn-O and Mn-Ca bonds exhibit changes associated with ordering of the structure (near T_R). Examination of the structure-function over the full temperature range reveals stiff Mn-O bonds and stiff Mn-Mn correlation with weak changes in the peak amplitudes with temperature (See Fig. S11) as predicted by the DFT simulations (Table I). The largest changes with temperature occur in the Ca-Mn correlation peak between 300 and 600 K. The Mn lattice sites are seen to form a very rigid network with major changes corresponding to the angular motion of rigid MnO_6 polyhedra units and the Ca ions. In the temperature region between 300 and 700 K (Fig. S12), an enhancement of the Mn-O peak width is seen near 400 K on warming.

Examination of the Ca site (Ca-O, Ca-Mn and Ca-Ca bonds up to $\sim 4 \text{ \AA}$) near the vicinity of the transition at 400 K reveal an enhancement of Ca-Mn correlation (peak width of Ca-Mn distribution) on heating through T_R indicating an increase on local symmetry at this transition. This can be seen in Figs. S13 and Table S2, where the Gaussian width of the Ca-Mn are found to become narrow on going above the T_R .

To follow the local structure trends in the X=Ti system, Ti K-edge XANES spectra of crystal derived $\text{Ca}_{2.4}\text{Sr}_{0.6}\text{Ti}_2\text{O}_7$ samples were measured for temperatures between 300 and 540 K (Fig. S14(a)). It was found that the main pre-edge feature (feature B in Fig S14(b)) increases in intensity with increasing temperature. Simulated XANES spectra for perovskite systems (Fig. S14(b)) showed that the reduction of tilting amplitude relative to the long axis (called a-axis here) increases the amplitude of peak B while reduction of twisting about z-axis reduces the peak amplitude (dotted line). Hence the observed continuous increase the B feature amplitude for temperatures from 300 to 540 K is related to a continuous

loss of tilt angle with temperature. Hence, like the $\text{Ca}_3\text{Mn}_2\text{O}_7$ system, the $\text{Ca}_{2.4}\text{Sr}_{0.6}\text{Ti}_2\text{O}_7$ (representing X=Ti) system shows a reduction in tilt angle with increasing temperature.

V. Nanoscale Structural Measurements (X-Ray Pair Distribution Function Analysis)

More detailed structural information on $\text{Ca}_3\text{Mn}_2\text{O}_7$ and $\text{Ca}_3\text{Ti}_2\text{O}_7$ type systems was obtained on an intermediate length scale by PDF measurements between 100 K and 1100 K (in real space taken over the range 1.3 to 20 Å (Fig. S15), single crystal based materials). To determine the space group in $\text{Ca}_3\text{Mn}_2\text{O}_7$ on this intermediate structural level on crossing the transition near 400 K (T_T), fits to unit cells with possible space groups suggested previously [3] were examined including the groups $\text{Cmc}2_1$ (#36), $\text{Amm}2$ (#38), Amam (#63), Acam (#64), and Acaa (#68). The R_W parameter indicating the fit quality was compared over the temperature range 200 to 450 K for each space group (see Fig. S16(a)). ($R_W = \left\{ \frac{\sum_{i=1}^N w(r_i)[G_{Obs}(r_i) - G_{Calc}(r_i)]^2}{\sum_{i=1}^N w(r_i)[G_{Obs}(r_i)]^2} \right\}$ was scaled by the number of independent parameters minus the number of free fitting parameters [11]). Additional, comparisons of the space group $\text{Cmc}2_1$ (#36) with the nonpolar space group $\text{I4}/\text{mmm}$ (#139) and $\text{C2}/\text{m}$ (#12, see below), both with cells having $\frac{1}{2}$ the volume of the $\text{Cmc}2_1$ unit cell, were also conducted (Fig. S16(b)). The results indicate that below (T_T), $\text{Ca}_3\text{Mn}_2\text{O}_7$ crystals possess $\text{Cmc}2_1$ space group symmetry on an intermediate structural range. While above it, the space group is closer to the $\text{C2}/\text{m}$ space group on this intermediate length scale (1.3 to 20 Å used in fits). Examining the a/c ratio (Fig. S17) reveals an abrupt transition near 400 K on warming and near 370 K on cooling consistent with the DSC measurements (Fig. 3). The high temperature PDF measurement over the range 300 to 1100 K (Fig. S18) reveals an abrupt change in R_W near 1060 K and smooth increase in the b/c ratio at this transition but no change along the c axis consistent with rotation of the MnO_6 polyhedra (T_R).

In Fig. 6. we examine the change in the structure of $\text{Ca}_3\text{Mn}_2\text{O}_7$ on this length scale in more detail (with respect to the cell $\text{Cmc}2_1$ cell in Fig 1). In Fig. 6(a), the volume on cooling (3 K steps) reveals two

distinct regions of thermal expansion behavior. The volumetric thermal expansion coefficient (α_V) takes on the value $3.5(1) \times 10^{-5} \text{ K}^{-1}$ above $\sim 370 \text{ K}$ and the value $2.63(4) \times 10^{-5} \text{ K}^{-1}$ below it. Near 110 K evidence is seen for a negative thermal expansion corresponding to the onset of the magnetic ordering and spin lattice coupling. The inset of the figure reveal hysteresis behavior covering the region between ~ 350 and $\sim 400 \text{ K}$. (Consistent with earlier published work on polycrystalline samples [4], our PDF data on polycrystalline samples (Fig. S19, inset) reveals hysteresis behavior covering a much broader region of temperature (~ 250 to $\sim 400 \text{ K}$.) As indicated in Fig. 6(b), examination of the PDF refinement xyz data indicates that the Mn x position (long axis) show abrupt change both at T_N and at T_T . However, the Ca x atomic position show changes only at T_T . With the enhanced symmetry indicated by the XAFS results on the Ca local structure, this indicates a loss of polarization at T_T . The exact nature of the structural change was qualitatively determined by looking at the atomic displacements of the 400 K PDF structure relative to the structure at 300 K . In Fig 6(c), we see that the major displacements are for axial O atoms leading to reduction of the MnO_6 tilt amplitude (X_3^- amplitude).

VI. Single Crystal Diffraction Measurements (Space Group above T_T)

Accurate structural parameters of $\text{Ca}_3\text{Mn}_2\text{O}_7$ were derived from detailed synchrotron single crystal diffraction measurements on ~ 20 microns crystals between 300 and 480 K on warming. A high count rate Pilatus 1M detector (10^7 cps maximum/pixel) was utilized to obtain large signals for structure factors corresponding to scattering from both the light O atoms and heavy atoms (Mn/Ca). (Use of this detector with the high flux at a synchrotron beamline was found to enable the structural solution of atomic positions of B atoms in rare earth systems such as $\text{HoAl}_3(\text{BO}_3)_4$ yielding accurate B-O distances (see Ref. [12]).) For each temperature data set, a systematic space group search was conducted [13]. Fits of full diffractions data sets on the $\text{Cmc}2_1$ structure were found to be stable for the temperature range 300 (fit parameter $R1 = 5.2\%$) to 380 K ($R1 = 5.6\%$). At 400 K the best structural refinements were obtained for the nonpolar spacegroups $\text{I}4/\text{mmm}$ ($R1 = 5.6\%$) and $\text{C}2/\text{m}$ ($R1 = 7.1\%$). Fits to the polar $\text{Aba}2$ space

group at 400 K yielded $R1 = 10\%$ and large residual charge density. Measurements up to 480 K were taken, and the fits to $I4/mmm$ and $C2/m$ space groups yielded $R1 = 4.2\%$ and $R1 = 4.8\%$, respectively.

The full structural data from the refinements of $Ca_3Mn_2O_7$ at 480 K are given in Tables S3 and S4 for $I4/mmm$ and Table S5 for the $C2/m$ space group (both with cells $\frac{1}{2}$ the $Cmc2_1$ cell). The room temperature structural data ($Cmc2_1$) are given in Tables S6 and S7. Tables S4 and S7 and Fig. S22 can enable comparison of the bond distribution difference between the 300 K and 480 K structures. The room temperature results reproduce the previously published work [14].

Using either of the high-temperature single crystal structure solutions ($I4/mmm$ or $C2/m$), it is found that the tilt angle in $Ca_3Mn_2O_7$ vanishes above T_T . Quantifying the result of Fig. 4(c), the X_3^- tilt amplitude vanishes and hence, the electric polarization determined by the existence of both X_3^- and X_2^+ distortion is predicted to vanish abruptly near 400 K on heating. The single crystal results are consistent with the abrupt in-plane shift at the Ca site seen in the PDF measurement. Fig. 7 shows the 480 K structure ($I4/mmm$ space group) while the corresponding figure for $C2/m$ space group is given in Fig. S20. Note that in both structural solutions the rotation amplitude (X_2^+) is nonzero at 480 K. The in-plane O sites have double occupancy indicating the presence of 50/50 domains (by volume) with positive and negative in plane rotations (X_2^+ mode) of the MnO_6 polyhedra but of the same magnitude (see structural results in Tables S3 and S5). It should be noted that the abrupt change in structure and loss of tilt seen in the single crystal measurements are consistent with first order behavior seen in the DSC and Raman measurements as well as with the abrupt changes in structure found in the PDF refinements. **The electric polarization in $Ca_3Mn_2O_7$ is expected to vanish abruptly near T_T while that in $Ca_3Ti_2O_7$ is expected to vanish continuously after passing through T_T .**

VII. High Pressure Raman Measurements

To understand the softness of the tilting configuration in the $\text{Ca}_3\text{Mn}_2\text{O}_7$ system quantitatively, high-pressure Raman scattering measurements were conducted. In Fig.8, data are shown for the pressure range 1 to 13.4 GPa for the same crystal orientation as in Fig. 3. The feature near 140 cm^{-1} , labeled A (Fig. 8(a)), is seen to vanish between 1.4 and 2.3 GPa. In temperature-dependent ambient pressure Raman measurements (Fig. 2), this feature was associated with the loss of tilt and transition into a nonpolar phase as indicated by the combined structural and optical measurements. We find that at very low pressures, the system goes from the $\text{Cmc}2_1$ space group into a nonpolar space group ($\text{C}2/\text{m}$). Between 4.7 and 5.8 GPa (inset, Fig. 8(a)) the peak near 380 cm^{-1} splits into two components and an additional feature near 190 cm^{-1} onsets and grows larger as pressure rises (indicating symmetry reduction). Fig. 8(b) and the corresponding inset again shows the disappearance of the same feature between 1.4 and 2.3 GPa (near 460 cm^{-1}) which vanishes at T_T in the ambient pressure data (Fig. 3).

VIII. Discussion of Combined Results

Development of an intuitive approach for the origin of the softness of the tilt mode is possible via simulations. The DFT derived self-force constants [15] (on site terms in force constant matrix which indicate the force on the isolated atom with respect unit displacements) are presented in Table I for each unique site the directions are labeled by the unit cell in Fig. 1 (for both $\text{Ca}_3\text{Mn}_2\text{O}_7$ and $\text{Ca}_3\text{Ti}_2\text{O}_7$). The force constants of the Mn sites are seen to be the same for displacements along a, b, and c axis for the Mn sites. They are also significantly larger than those of any other atomic sites. Combined with typically strong Mn-O bonds, the results predict rigid MnO_6 polyhedra. For the apical O sites, the force constants in the yz plane are smaller than those for motion transverse to this plane ($k_x, k_z \sim 1/3 k_x$ (long axis)). The same holds for the apical interior O atoms. On the other hand, the planar (O3, O4) atoms have ($k_x, k_z \sim 2 k_x$). This predicts that local tilting (Fig. 1(b)) of the MnO_6 polyhedra corresponding mainly to y/z displacement of the apical O and displacement of the planar O atoms will be softer than rotation of the

polyhedra about the x-axis (long axis). In the case of the rotation, the planar O atoms have $k_x, k_z \sim 2 k_x$ making this type of distortion relatively stiffer. The same trend in self-force constants is seen for the $\text{Ca}_3\text{Ti}_2\text{O}_7$ system. **Hence it is predicted that local tilting of single MnO_6 polyhedron in the lattice, as opposed to coherent long-range tilting of all MnO_6 polyhedra simulated in previous work [3], is a lower energy distortion than local rotation in both $\text{Ca}_3\text{Mn}_2\text{O}_7$ and $\text{Ca}_3\text{Ti}_2\text{O}_7$.** Also, in contrast with the current work, Ref. [9] suggests a difference in behavior between $\text{Ca}_3\text{Mn}_2\text{O}_7$ and $\text{Ca}_3\text{Ti}_2\text{O}_7$ with enhancement of both antiphase tilt and in-plane rotation occurring with increasing temperature in $\text{Ca}_3\text{Ti}_2\text{O}_7$, this is not observed in this work.

In addition to the possibility of local tilt or local rotation structural phases being the cause of the observed order of the transitions, we note that the relative stability of the X_3^- and X_2^+ distortions is reversed by compressive biaxial strain of $\sim 1.5\%$ [3] compared to the strain free or tensile strained systems under DFT+U. This strain value is at the level of accuracy for the determination of lattice parameters found in standard DFT simulations. It would be useful to explore more accurate methods than DFT+U to determine the stable structural phases.

IX. Summary

We note that the $\text{Ca}_3\text{Mn}_2\text{O}_7$ and $\text{Ca}_3\text{Ti}_2\text{O}_7$ exhibit a transition near 400 K with verified loss of inversion center in the case of $\text{Ca}_3\text{Mn}_2\text{O}_7$ (for temperatures below ~ 400 K). The characteristic feature in these systems is the low energy **local tilting** of the Mn/Ti- O_6 polyhedra groups. To sustain the electric polarization at higher temperatures, it is necessary to strengthen the bond on the Ca site (A site) in these systems. We also note that the low isotropic pressure needed to suppress the polarization state (1-2 GPa) will be significantly reduced if uniaxial pressure is applied. This may make it possible to switch the electrical polarization on and off by depositing this material as a thin film on a piezoelectric substrate for films strained just below this critical strain value. The measurements also suggest that simulations beyond standard DFT+U may be needed to determine the ordering of the energetics of the distortions.

X. Acknowledgments

This work is supported by NSF Grant No. DMR-1809931. Work at Rutgers University is supported by DOE Grant No. DE-GF02-07ER46382. This research used resources of the National Synchrotron Light Source, a U.S. Department of Energy (DOE) Office of Science User Facility operated for the DOE Office of Science by Brookhaven National Laboratory under Contract No. DE-AC02-98CH10886. Single crystal x-ray diffraction measurements were performed at NSF's ChemMatCARS Sector 15, which is principally supported by the National Science Foundation/Department of Energy under Grant NSF/CHE-1346572. Use of the Advanced Photon Source was supported by the U.S. Department of Energy, Office of Science, Office of Basic Energy Sciences, under Contract No. DE-AC02-06CH11357. The Physical Properties Measurements System was acquired under NSF MRI Grant DMR-0923032 (ARRA award). This research used resources of the National Energy Research Scientific Computing Center, a DOE Office of Science User Facility supported by the Office of Science of the U.S. Department of Energy under Contract No. DE-AC02-05CH11231.

Table I. $\text{Ca}_3\text{Mn}_2\text{O}_7$ and $\text{Ca}_3\text{Ti}_2\text{O}_7$ Self-Force Constants

Ion Site	k_x (long axis) (eV/Å ²)	k_y (eV/Å ²)	k_z (eV/Å ²)
$\text{Ca}_3\text{Mn}_2\text{O}_7$			
Mn	26	26	26
Ca1	8.6	7.9	7.7
Ca2	11	7.5	6.8
O1 (apical interior)	21	8.8	5.7
O2 (apical)	17	6.6	5.4
O3	7.2	14	15
O4	7.6	14	14
$\text{Ca}_3\text{Ti}_2\text{O}_7$			
Ti	24	19	19
Ca1	8.0	6.8	6.3
Ca2	11	7.8	6.7
O1 (apical interior)	21	8.1	6.0
O2 (apical)	18	6.8	5.2
O3	7.6	13	15
O4	8.1	13	13

Figure Captions

Fig. 1. (a) Low-temperature unit cell indicating unique O sites and (b) the MnO_6 polyhedral rotation about the long axis (X_2^+ , black curved arrow) and the tilts (X_3^- , blue arrows) of the polyhedra normal to the long axis. (c) Partial density of states derived from DFT simulations showing the Mn, Ca and O site projected components. Note that the phonon DOS corresponding to the Ca sites vanishes for energies above $\sim 350 \text{ cm}^{-1}$.

Fig. 2. (a) Raman spectra of single crystal for photon beam normal to the long axis for data taken between 100 and 500 K. Note that the weak peak near $\sim 146 \text{ cm}^{-1}$ vanishes as temperature increases (measured on cooling from 500 K). The vertical line indicates the abrupt change in structure near 370 K (b) The weak peak (arrow in (a)) area vs. temperature is displayed showing that it disappears above $\sim 370 \text{ K}$. (c) comparison of the peak position vs. temperature for the main Raman peak for powder and single crystal samples. Data are for cooling unless both warming and cooling results are shown.

Fig. 3. DSC curves for $\text{Ca}_3\text{Mn}_2\text{O}_7$ (cooling rate= 20 K/min) from single crystal materials. Multiple scans reveal the high reproducibility of the transitions in both systems. The hysteresis in the complete loops (see offset transitions here at 405 K on warming and 367 K on cooling) reveal that the transition in $\text{Ca}_3\text{Mn}_2\text{O}_7$ is first order.

Fig. 4. XAFS structure function of $\text{Ca}_3\text{Mn}_2\text{O}_7$ measured between 320 K and 1100 K (in (a) and (b)) revealing that the Mn-Mn first and second nearest neighbor in plane correlations persist for the full temperature range. In (b) the inset shows that there is an abrupt reduction of the position of the Mn-O peak near 1060 K indicating the transition to the $I4/mmm$ high symmetry structure.

Fig. 5. Local structure results derived from XAFS measurements. In the high-temperature region the (a) Mn-O and (b) Mn-Ca bond lengths reveal abrupt changes near 1060 K.

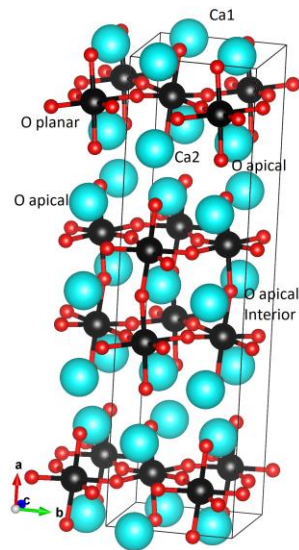
Fig. 6. Intermediate structure results derived from PDF measurements. (a) Temperature-dependent volume (cooling data) with b axis length shown as inset (warming and cooling). Clear transitions are seen near ~350 K on cooling and near ~400 on warming (b-axis). The volume data also reveal a transition near 105 K which is the magnetic ordering temperature (see also heat capacity data in Fig S1). (c) Position of the Ca₂ and Mn ions vs. temperature revealing that only the Mn site position changes near 105 K and both Mn and Ca sites change near 370 K (cooling run). Motion of ions going from 300 K to 400 K. The arrows indicate exclusively a tilt rotation about an axis normal to the long axis exclusively.

Fig. 7. Crystal structure at 480 K derived from single crystal diffraction data. Note that the tilt angle vanishes. The planar oxygen atoms exist in two positions with 80 % probability indicating multiple domain structure but the rotation about the local z-axis is nonzero relative to the cubic structure.

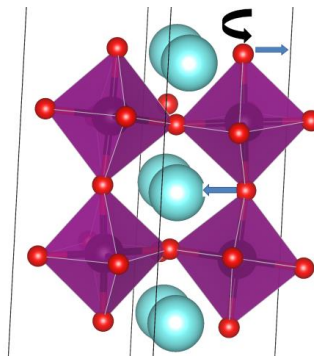
Fig. 8. High-pressure Raman measurements for the incident beam normal to (a) and parallel to (b) the long axis. High-pressure Raman data reveal a phase transition between 1.0 and 2.3 GPa indicated by suppression of features A and D in panels (a) and (b). The feature D is expanded in the inset to panel (b). Panel (a) shows a second transition onsetting near 5.8 GPa as feature labeled B also associated with the splitting of a peak near 380 cm⁻¹ indicated as feature C.

Fig. 1. Liu *et al.*

(a)



(b)



(c)

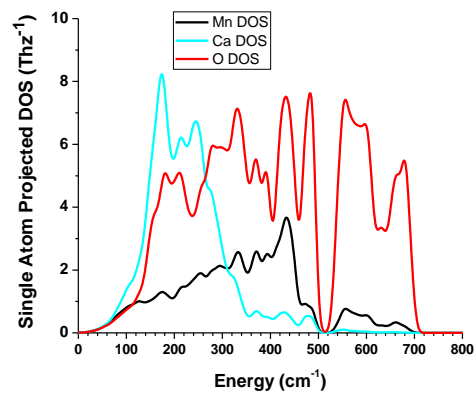
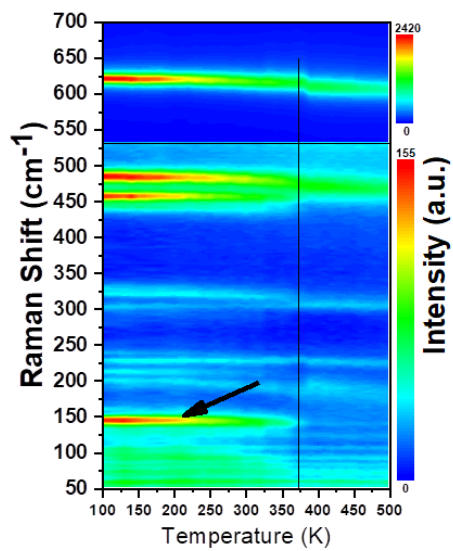
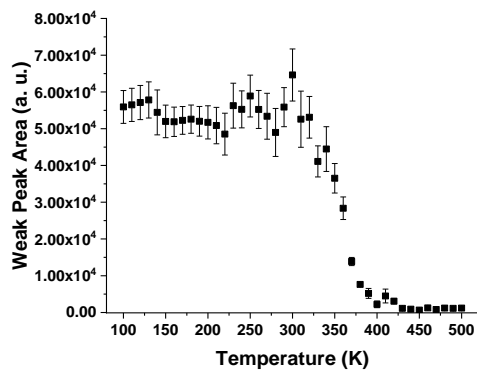


Fig. 2 Liu *et al.*

(a)



(b)



(c)

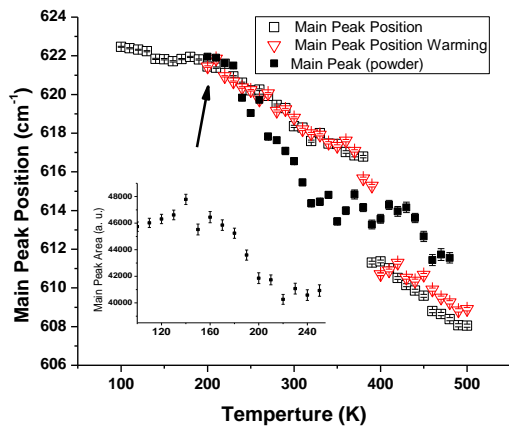


Fig. 3. Liu *et al.*

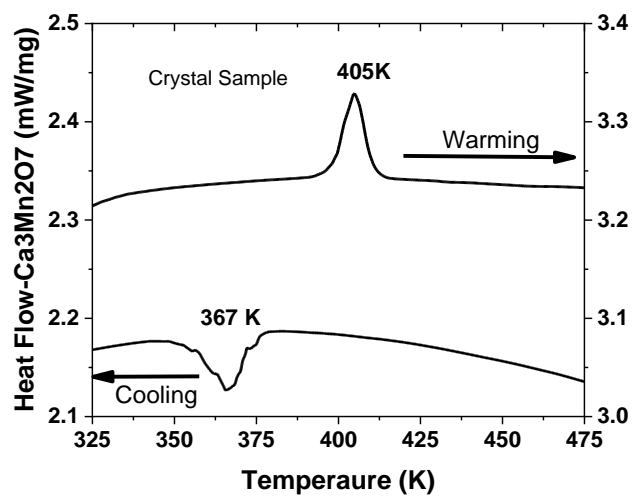


Fig. 4. Liu *et al.*

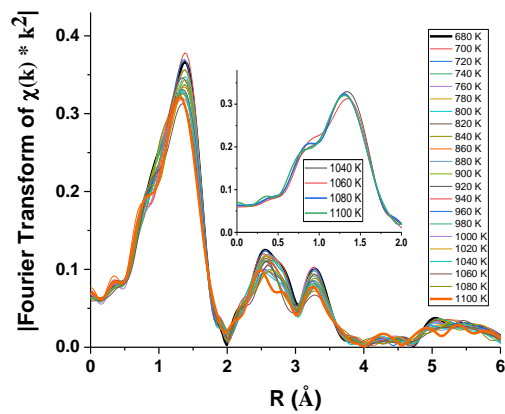
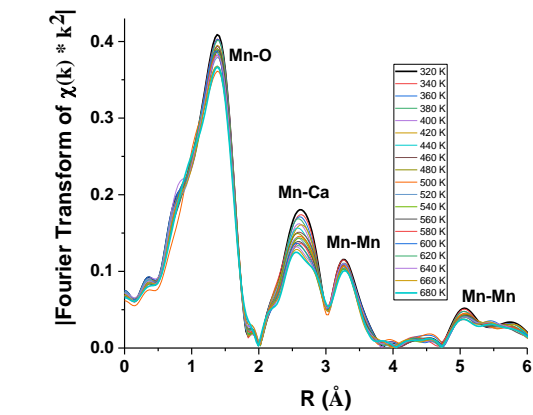


Fig 5. Liu *et al.*

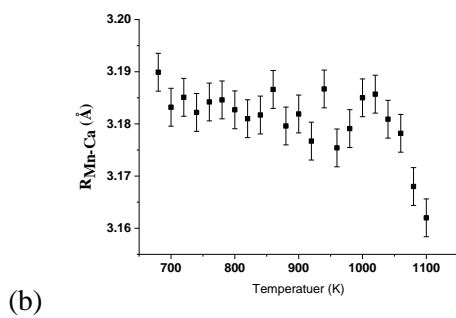
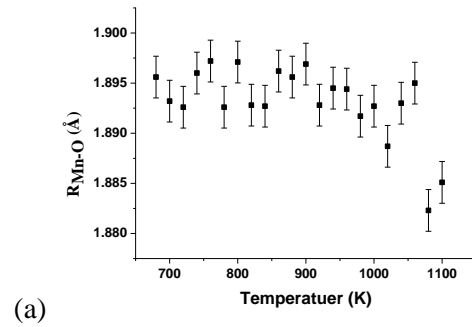
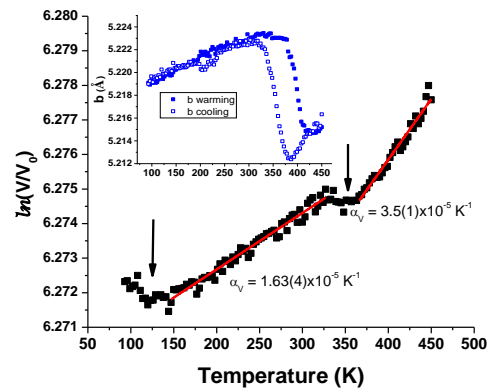
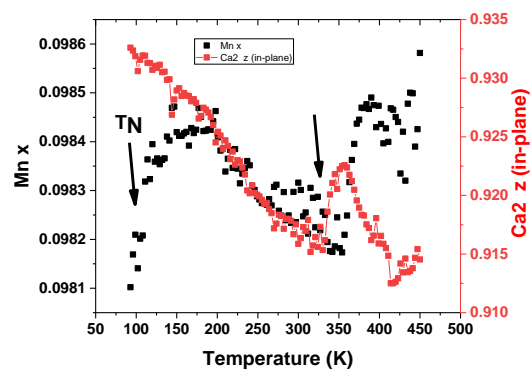


Fig 6. Liu *et al.*

(a)



(b)



(c)

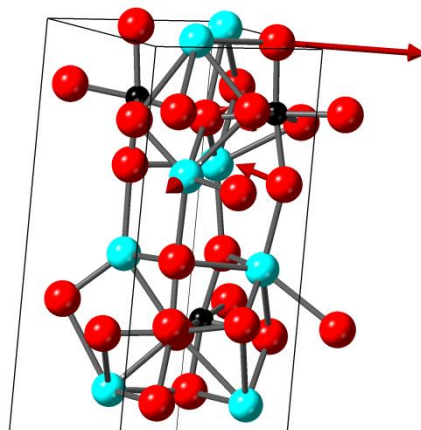


Fig 7. Liu *et al.*

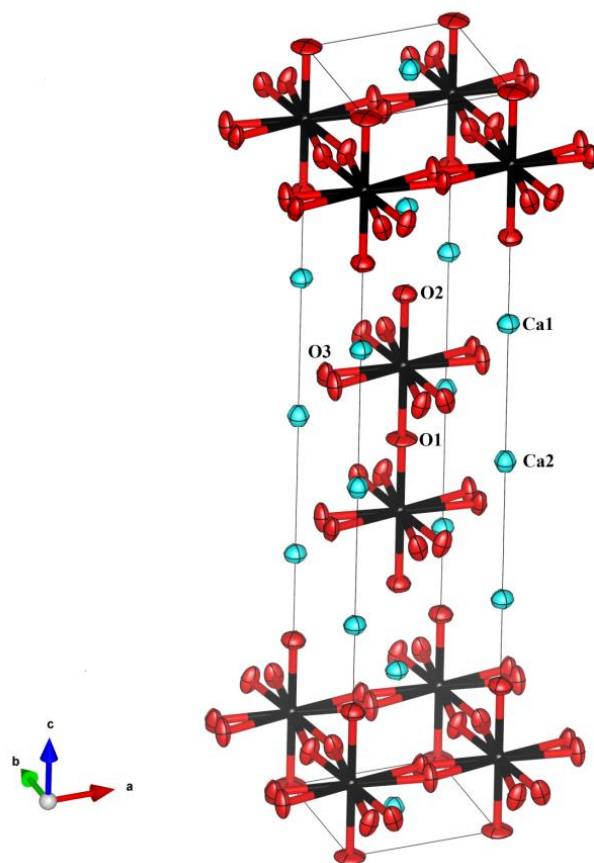
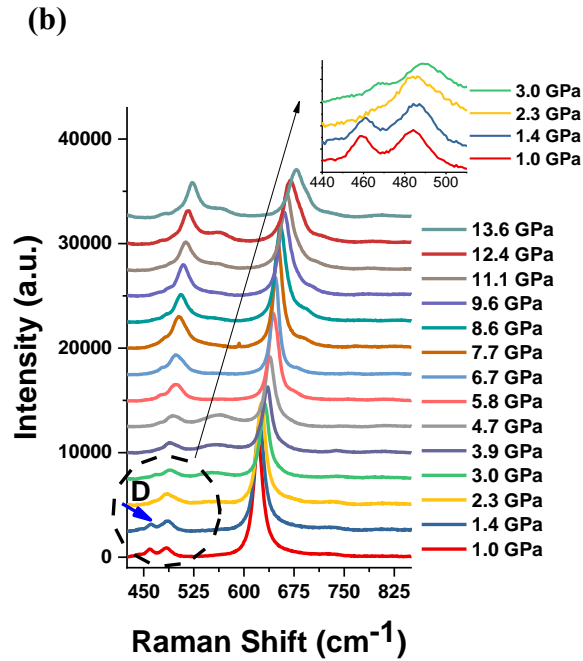
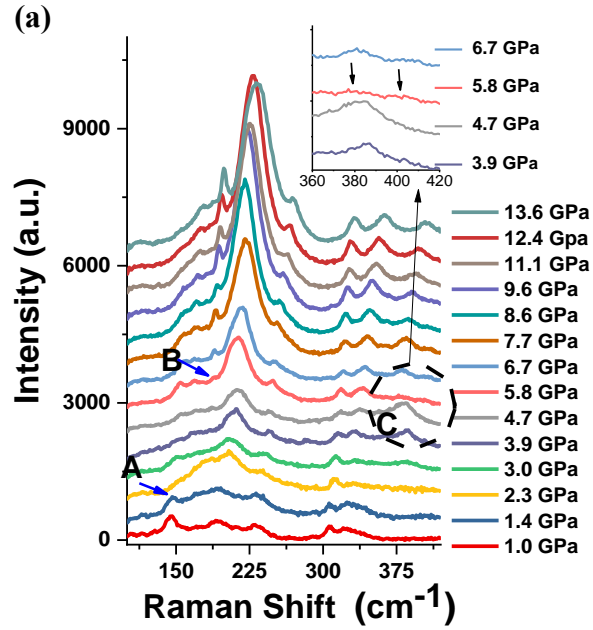


Fig. 8. Liu *et al.*



References

-
- [1] S. Picozzia and A. Stroppa, *European Physical Journal B* **85** (7), 240 (2012).
- [2] (a) M. Okuyama and Y. Ishibashi, *Ferroelectric Thin Films: Basic Properties and Device Physics for Memory Applications*, (Springer, Berlin, 2005).
- (b) M. Dawber, K. M. Rabe, J. F. Scott, *Rev. Mod. Phys.* **77**, 1083 (2005).
- (c) M. T. Dove, *American Mineralogist* **82**, 213 (1997).
- [3] N. A. Benedek and C. Fennie, *Phys. Rev. Lett* **106**, 107204 (2011).
- [4] A. Harris, *Phys. Rev. B* **84**, 064116 (2011).
- [5] M. S. Senn et al., *Phys. Rev. Lett.* **114**, 035701 (2015).
- [6] B. Gao et al., *Appl. Phys. Lett.* **110**, 222906 (2017).
- [7]] Y. S. Oh, X. Luo, F.-T. Huang, Y. Wang, S.-W. Cheong, *Nat. Mater.* **14**, 407 (2015).
- [8] A. Galmazada, D. Wulfreding, P. Lemmens, B. Gao, S.-W. Cheong, and K.-Y. Choi, *Phys. Rev. B* **97**, 094104 (2018).
- [9] F. Ye, J. Wang, J. Seng, C. Hoffmann, T. Gu, H. J. Xiang, W. Tian, J. J. Molaison, A. M. dos Santos, M. Matsuda, B. C. Chakoumakos, J. A. Fernandez-Baca, X. M. Tong, B. Gao, J. W. Kim, S.-W. Cheong., *Phys. Rev. B* **97**, 04112 (2018).
- [10] L.-F. Huang, X.-Z. Lu and J. M. Rondinelli, *Phys. Rev. Lett.* **117**, 1159011 (2016).
- [11] T. Egami and S. L. J. Billinge, *Underneath the Bragg Peaks: Structural Analysis of Complex Materials*, (Pergamon, Amsterdam, 2003), P. 232.
- [12] H. Zhang, S. Liu, C. Nelson, L.N. Bezmaternykh, Y-S. Chen, S. G. Wang, R.P.S.M. Lobo, K. Page, M. Matsuda, D. M. Pajeroski, T. J. Williams and T. A. Tyson¹, submitted to *Phys. Rev. B*
- [13] Systematic space group searches were conducted using the integrated methods in SHELXT and PLATON. (a) G. M. Sheldrick, *Acta Cryst* **A71**, 3 (2015). (b) A. L. Spek, *Acta Cryst.* **D65**, 148 (2009).
- [14] N. Guiblin, D. Grebille, H. Leligny and C. Martin, *Acta Cryst* **C58**, i3 (2001).
- [15] Ph. Ghosez, E. Cockayne, U. V. Wagjmare, and K. Rabe, *Phys. Rev. B* **60**, 836 (1999).

Nature of the Structural Symmetries Associated with Hybrid Improper Ferroelectricity in $\text{Ca}_3\text{X}_2\text{O}_7$ (Supplementary Document)

S. Liu¹, H. Zhang¹, S. Ghose^{2,*}, M. Balasubramanian³, Zhenxian Liu⁴, S. G. Wang⁵, Y-S. Chen⁵, B. Gao^{6,7},
J. Kim^{6,7}, S.-W. Cheong^{6,7}, B. Nowadnick^{1,7}, and T. A. Tyson^{1,7,*}

¹Department of Physics, New Jersey Institute of Technology, Newark, NJ 07102

²National Synchrotron Light Source II, Brookhaven National Laboratory, Upton, NY 11973

³Advanced Photon Source, Argonne National Laboratory, Argonne, IL 60439

⁴Institute of Materials Science, Department of Civil and Environmental Engineering,
The George Washington University, Washington, DC 20052

⁵Center for Advanced Radiation Sources, University of Chicago, Argonne, IL 60439

⁶Department of Physics and Astronomy, Rutgers University, Piscataway, NJ 08854

⁷Rutgers Center for Emergent Materials, Rutgers University, Piscataway, NJ 08854

*Corresponding Authors: T. A Tyson, e-mail: tyson@njit.edu
S. Ghose, e-mail: sghose@bnl.gov

Samples of $\text{Ca}_3\text{Mn}_2\text{O}_7$ and $\text{Ca}_{3-x}\text{Sr}_x\text{Ti}_2\text{O}_7$ were prepared in single crystal form as given in Ref. [1]. For powder sample measurements, the crystal samples were crushed in 500 mesh powders. Polycrystalline samples prepared by solid-state reaction were also examined for comparison, but the primary work is on materials derived from single crystal samples.

Specific heat measurements on single crystals were conducted on cooling from 390 K to 2 K and on warming from 60 K to 390 K using the relaxation method in a Quantum Design PPMS system. Temperature steps of 1 K were utilized, and each temperature point was measured three times, and the average result is reported (Fig. S1). Approximately 10 minutes was required to measure each temperature data point. Hence the system was never in a quenched state. Differential scanning calorimetry measurements were conducted under flowing N_2 using a Perkin Elmer DSC 6000. Ambient pressure Raman Spectra were measured with an excitation wavelength of 532 nm in backscattering geometry using a Thermo Scientific DXR Raman Microscope. A 50X objective was used with 10 mW power setting. The sample was found to be stable under this laser power after test were done on a range of laser powers (3 to 10 mW). The original spectra were recovered after warming and cooling cycles. Both the Raman and DSC measurements were conducted at the NJIT York Center.

High-pressure Raman measurements were conducted at National Synchrotron Light Source (NSLS2) beamline 22-IR-1 National . Measurements were conducted in a symmetric diamond cell with (100) oriented diamonds. The culet size was 500 μm and tungsten gaskets were used. The pressure medium utilized was methanol:ethanol:water in a 14:3:1 ratio by volume. Pressure calibration was conducted using both ruby fluorescence mainline shifts [2] and the changes in the diamond Raman edge (near $\sim 1300\text{ cm}^{-1}$) [3]. Pressure calibration measurements were made before and after each Raman spectrum was collected. In addition, calibration measurements as a function of position at multiple points in the cell at the highest pressure showed variation below 0.1 GPa indicating a high level of hydrostatic behavior of the pressure medium. The custom micro-Raman system at beamline 22-IR-1 consisted of a 532 nm solid-state laser (Spectral-Physics Excelsior, 150 mW), a Princeton Instruments liquid-nitrogen cooled PyloN CCD detector, a PI Acton SpectraPro SP-2556 Imaging Spectrograph and a 50X objective.

Based on the ambient pressure laser power tests, a laser power was used which caused no change in sample spectra during the measurements. The accumulation time was 20 seconds and averaged 20 times. For all Raman measurements no change in the spectra was observed over time at a given pressure.

Diffraction measurements on ~ 20 μm diameter crystals were conducted at the Advanced Photon Source (Argonne National Laboratory) beamline 15-ID-B with a wavelength of 0.41328 \AA . The data were collected with a PILATUS 1M detector (maximum count rate = 10^7 cps/pixel, counter depth = 20 bit) between 300 K and 480 K. Refinement of the data was done using the program Olex2 [4] after the reflections were corrected for absorption. Anomalous scattering corrections were induced for all atoms.

To determine force constants and phonon DOS for $\text{Ca}_3\text{Mn}_2\text{O}_7$, spin density functional calculations in the projector augmented wave approach [5] were carried out utilizing the VASP code. Full structural optimization was conducted for both lattice parameters and atomic positions and the LDA+U approximation was implemented to obtain the relaxed structure. The parameters $U = 8.0$ eV and $J = 0.88$ eV were used for the Mn on-site coulomb and exchange parameters (as done for YMnO_3 [6]). An energy cutoff of 500 eV was implemented. The ground state structure was optimized so that forces on each atom were below 1×10^{-5} eV/ \AA . Force constants were determined using density functional perturbation theory. Cells of dimension $1 \times 1 \times 1$ (with 4 $\text{Ca}_3\text{Mn}_2\text{O}_7$ units) were utilized yielding DOS curves similar to the $1 \times 2 \times 2$ cell used in reference [7] for the $\text{Ca}_3\text{Ti}_2\text{O}_7$ system. The code Phonopy was utilized to determine the phonon density of states and phonon displacement mode from the force constants (see Fig 1, Fig. S1, Table I and Table S1) [8].

Mn and Ti K-edge XAFS spectra were collected at NSLS2 beamline 8-ID (ISS). Reduction of the x-ray absorption fine-structure (XAFS) data was performed using standard procedures [9]. Measurements were done in fluorescence mode with 500 mesh powders held in 1 mm quartz capillaries with 10 mm walls. Data were corrected for self-absorption. In the XAFS refinements, to treat the atomic distribution functions on equal footing, the Mn and Ti K-edge spectra were modeled in R-space by optimizing the integral of the product of the radial distribution functions and theoretical spectra with respect to the measured spectra. To treat the atomic distribution functions on equal footing at all temperatures the

spectra were modeled in R-space by optimizing the integral of the product of the radial distribution functions and theoretical spectra with respect to the measured spectra. Specifically, the experimental spectrum is modeled by, $\chi(k) = \int \chi_{th}(k, r) 4\pi r^2 g(r) dr$ where χ_{th} is the theoretical spectrum and $g(r)$ is the real space radial distribution function based on a sum of Gaussian functions ($\chi(k)$ is measured spectrum) [10] at each temperature (as in Ref. [11]). For each shell fit, the coordination number (N) was held at the crystallographic value but the position (R) and Gaussian width (σ) was fit to the data. For the Mn K-Edge, the k-range $2.50 < k < 12.1 \text{ \AA}^{-1}$ and the R-range $0.63 < R < 3.80 \text{ \AA}$ were utilized. Coordination numbers for the atomic shells were fixed to the crystallographic values. For the Mn K-Edge S_0^2 (accounting for electron loss to multiple excitation channels) value was fixed at 0.81. The Gaussian widths and positions were fit for each component. Additional Ca K-edge XAFS were collected at APS beamline 20 BM at Argonne National Laboratory. The measurements were done at 300 K, 350 K and 450 K. The k-range $2.39 < k < 10.4 \text{ \AA}^{-1}$ and the R-range $1.02 < R < 3.40 \text{ \AA}$.

The theoretical Ti K-edge x-ray near edge spectra (XANES) presented were computed, as in Ref. [12] using the RELXAS programs [13]. The potentials were computed for cubic perovskite structures, based on clusters containing the first 118 atoms surrounding the Ti site. A simple cluster based on CaTiO_3 was used to determine the changes in the XANES pre-edge structure on tilting and rotation of the TiO_6 polyhedra.

Pair distribution function experiments for all solid state reaction prepared powder samples were conducted at beamline the XPD (28 ID) beamline at Brookhaven National Laboratory's National Synchrotron Light Source II using a wavelength $\lambda = 0.18372 \text{ \AA}$ (67.486 keV). For the samples derived from single crystal $\text{Ca}_3\text{Mn}_2\text{O}_7$, measurements between 90 K to 450 K were conducted at APS beamline 6 ID-D at Argonne National Laboratory ($\lambda = 0.12368 \text{ \AA}$ (100.25 keV)). A high-temperature measurement set on crystal derived $\text{Ca}_3\text{Mn}_2\text{O}_7$ powder between 300 K and 1100 K was conducted at NSLS2 beamline 28 ID. All measurements utilized Perkin Elmer Area detectors with a sample to detector distance of ~200 mm. Exact detector to sample distances were derived by fit to Ni powder calibration standards. The

range $Q_{\min} = 0.23 \text{ \AA}^{-1}$ and $Q_{\max} = 25.1 \text{ \AA}^{-1}$ was used in data reduction. The methods utilized for analysis of the PDF data are described in detail in Refs. [1,14]. For the fits in R-space covered the range: $1.3 < r < 20 \text{ \AA}$. The time interval between temperature points was ~ 7 minutes. Combined with the small temperature steps, the approach kept the samples from being in quenched states.

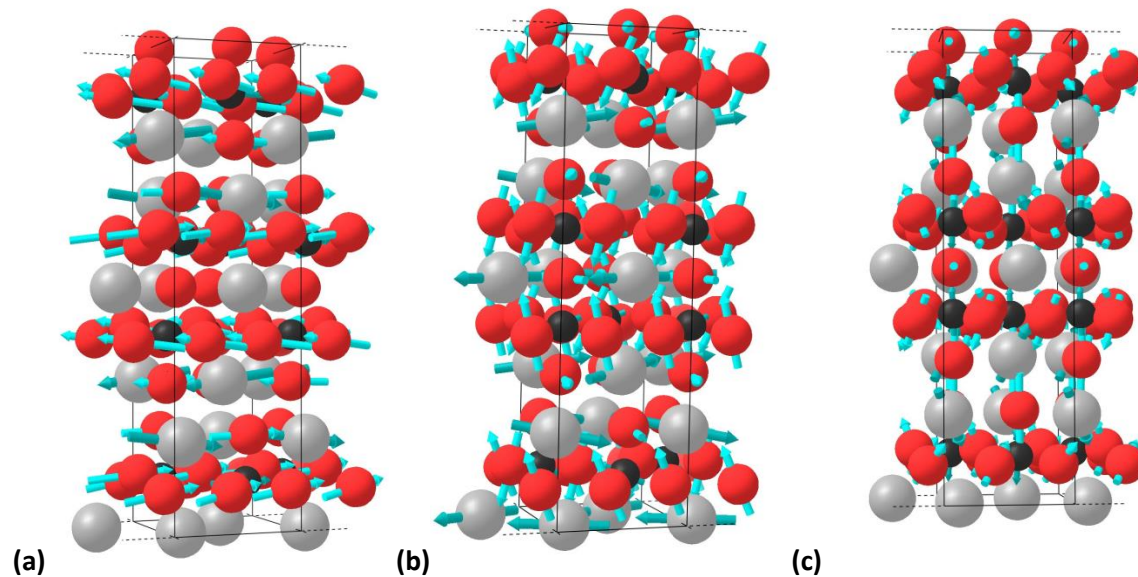
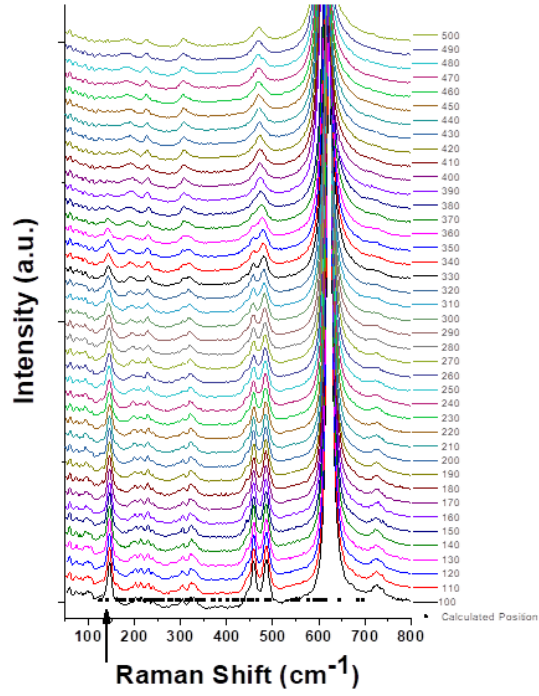


Fig. S1. Atomic motion for phonon modes from DFT simulations of $\text{Ca}_3\text{Mn}_2\text{O}_7$ for energies (a) 129, (b) 142 and (c) 612 cm^{-1} . The black, grey and red symbols correspond to Mn, Ca and O atoms. Note that the low-frequency modes involve motion of the Ca and O ions only. The arrows indicated the atomic displacement directions for one half of the motion cycle (arrows change direction on second half of cycle) with lengths indicating the corresponding amplitudes. The full set of phonon energies are given in Table S1.

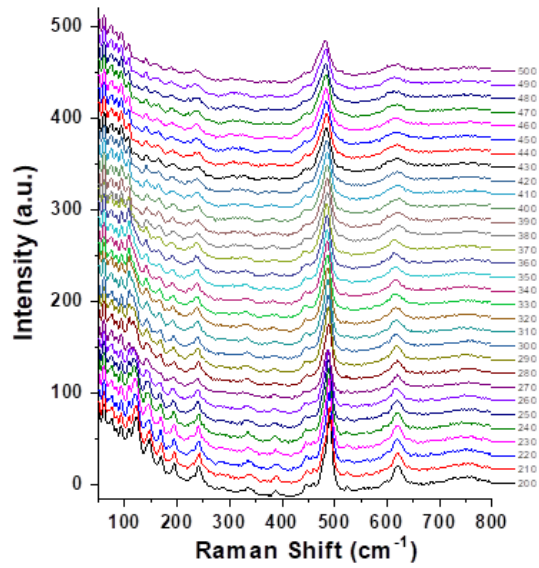
**Table S1. Computed Phonon Energies for $\text{Ca}_3\text{Mn}_2\text{O}_7$
($\text{Cmc}2_1$ Space Group)***

Energy(cm^{-1})	Irreducible Rep.	Energy(cm^{-1}) (cont.)	Irreducible Rep.
125.7	A1	333.2	A2
128.5	A1	338.5	B2
141.6	B2	344.3	B1
161.0	A2	350.1	A1
161.1	B2	370.2	A2
169.1	A1	372.6	A1
169.5	B1	385.1	B2
173.5	B2	402.6	B1
179.1	A2	414.5	A2
191.5	B1	422.5	B2
193.7	A2	434.7	A1
197.8	A1	436.7	B1
211.6	B2	437.2	B2
224.6	B1	446.1	A2
229.7	A2	451.7	B2
232.8	B1	456.1	A1
236.5	A1	465.8	B1
237.1	B2	485.8	A2
239.0	A1	492.6	A1
241.0	A2	493.2	B2
244.6	A1	540.6	A2
245.7	B2	546.0	B1
254.4	B1	555.0	B2
261.6	A2	576.9	A2
274.9	B2	590.1	B1
275.6	A1	595.2	A1
277.5	A2	604.4	B1
279.8	A1	604.7	A2
290.5	B1	605.4	A1
296.6	B2	611.3	B2
297.1	B1	615.2	A1
312.6	A1	644.9	B1
319.6	B2	683.3	B2
322.5	A1	695.8	A2
324.1	A1		

*The table shows that the calculation yielded 18 A1, 17 A2, 16 B1 and 18 B2 Modes.



(a)



(b)

Fig. S2. Full Raman spectra for $\text{Ca}_3\text{Mn}_2\text{O}_7$ single crystal for beam normal to (a) and along (b) the long axis (in-plane). The full spectrum is given in (a). Note the reduction in amplitude of the feature near 130 cm^{-1} indicated by the arrow. Data are from cooling curves.

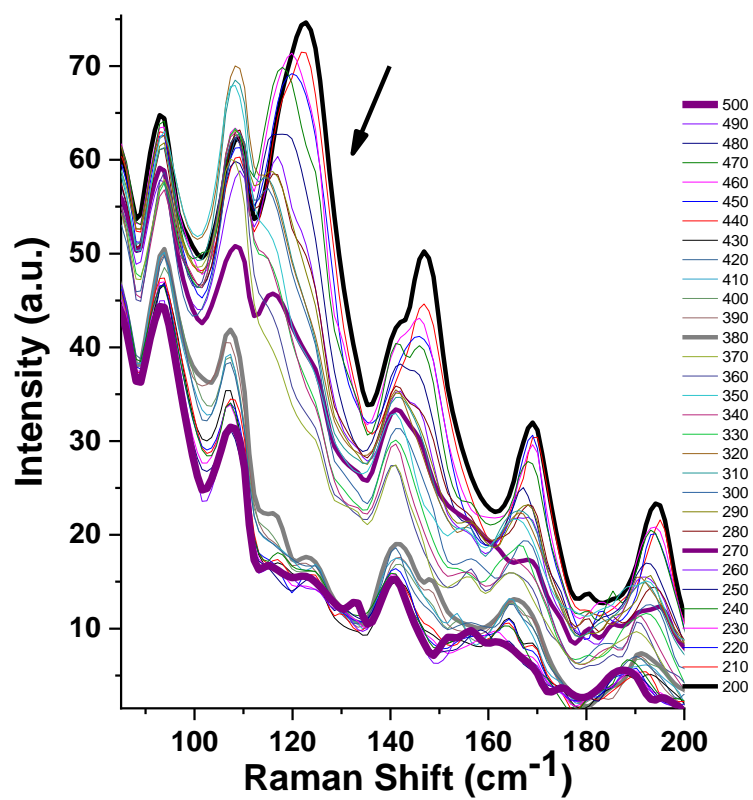


Fig. S3. Expanded low energy region Raman spectra for $\text{Ca}_3\text{Mn}_2\text{O}_7$ single crystal for beam along the long axis (in-plane). Note the reduction in amplitude of the feature near 120 cm^{-1} indicated by the arrow.

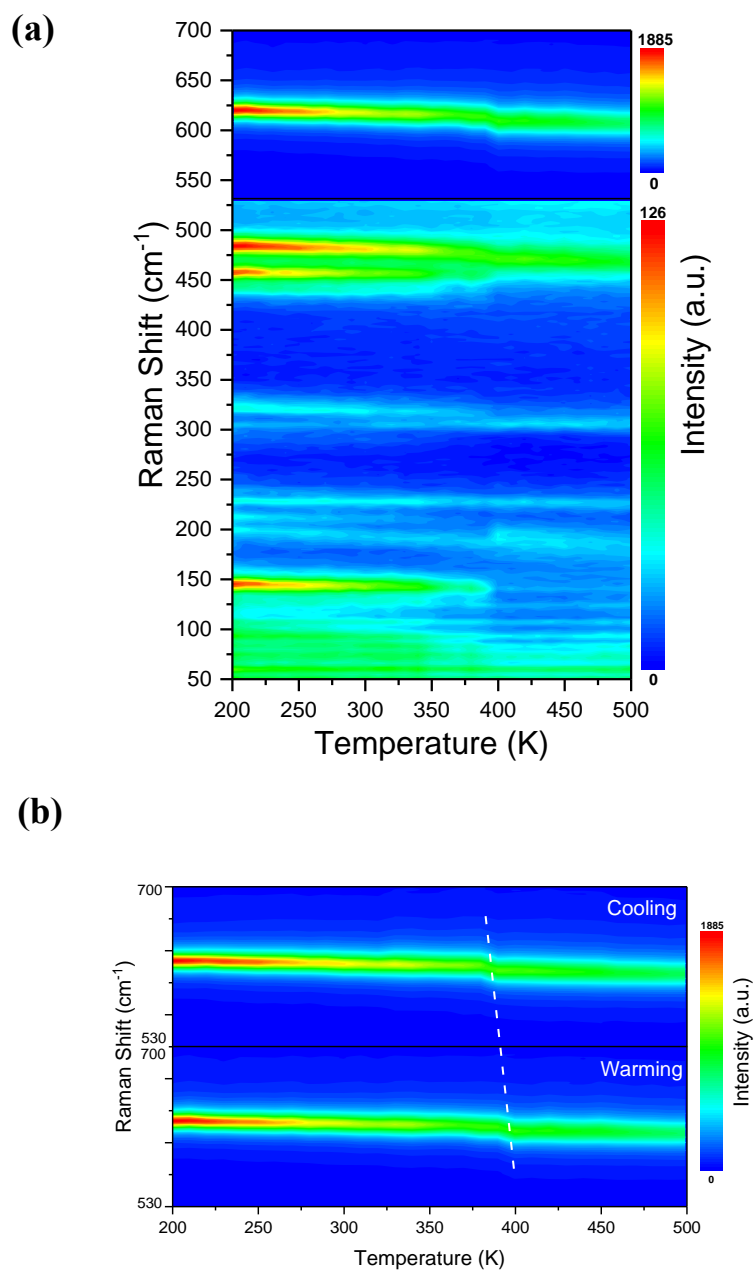


Fig. S4. (a) Surface plot for warming from 200 K to 500 K for incident beam normal to long axis. In (b), a surface plot is given for the intensity of the main peak vs. temperature for warming and cooling. As in Fig. 2, note the abrupt changes in the position of this peak near 370 K during cooling and near 400 K during warming.

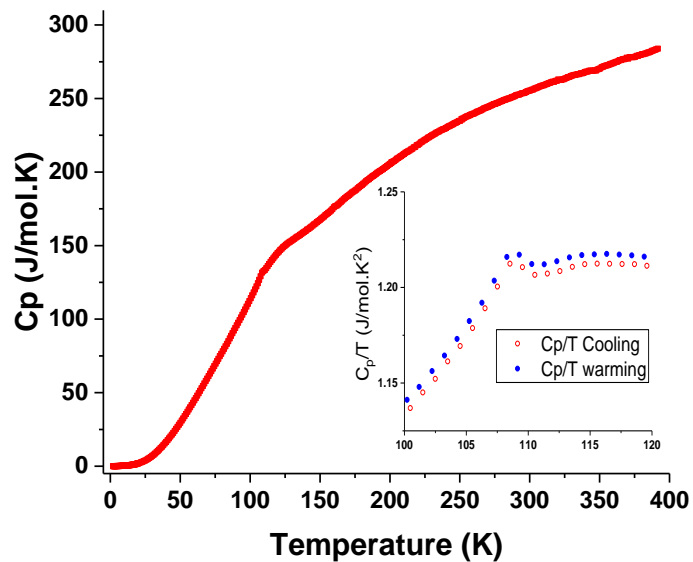


Fig. S5. The heat capacity of $\text{Ca}_3\text{Mn}_2\text{O}_7$ single crystal revealing the magnetic transition near ~ 108 K (see inset). Note that no additional clear features are seen up to the maximum temperature of 390 K indicating that any transition must be soft and/or continuous.

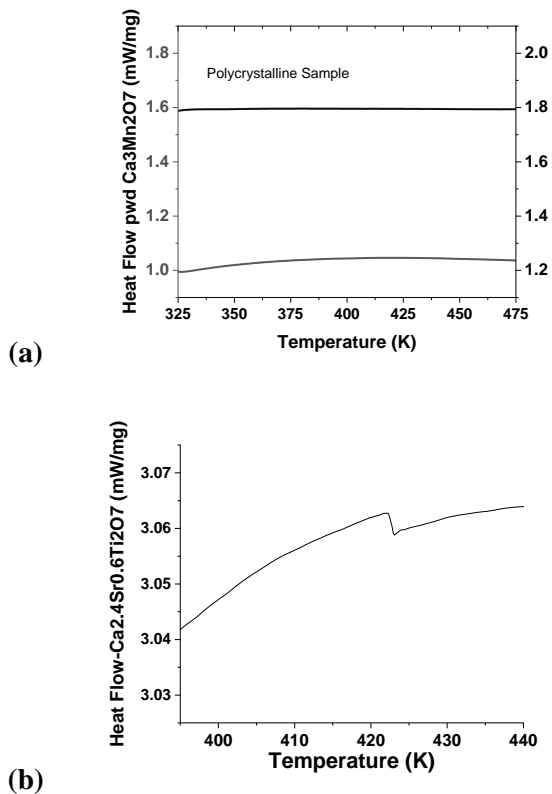


Fig. S6. (a) DSC curves for $\text{Ca}_3\text{Mn}_2\text{O}_7$ (cooling rate=20 K/min) from a polycrystalline sample (solid state synthesis) indicating no clear transition. Upper and lower curves have the same meaning as in (a). (b) Cooling curve DSC measurement for $\text{Ca}_{2.4}\text{Sr}_{0.6}\text{Ti}_2\text{O}_7$ crystals indicating a very weak feature characteristic with step change characteristic of a continuous or glass-like transition. Note that no background subtraction (of Al container) was done for samples.

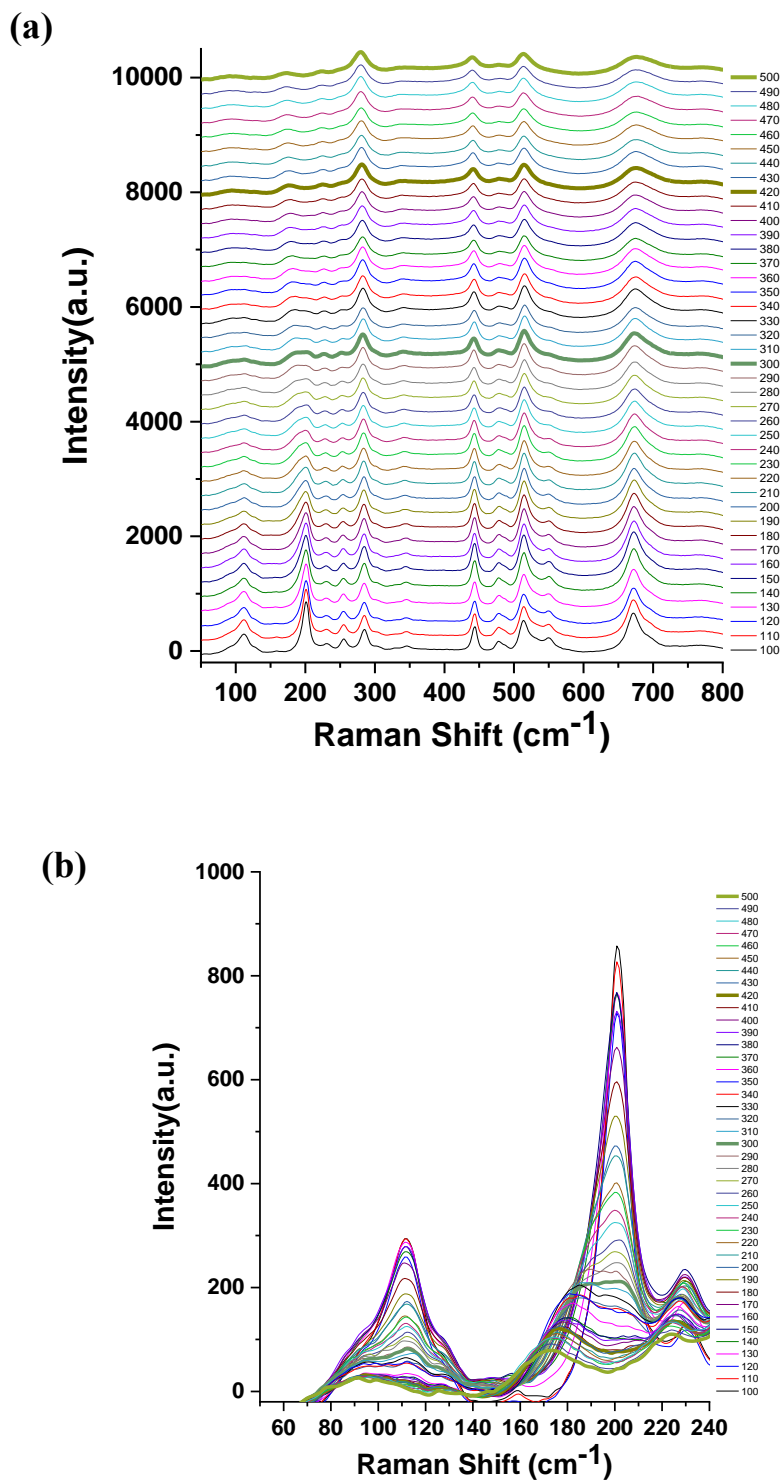
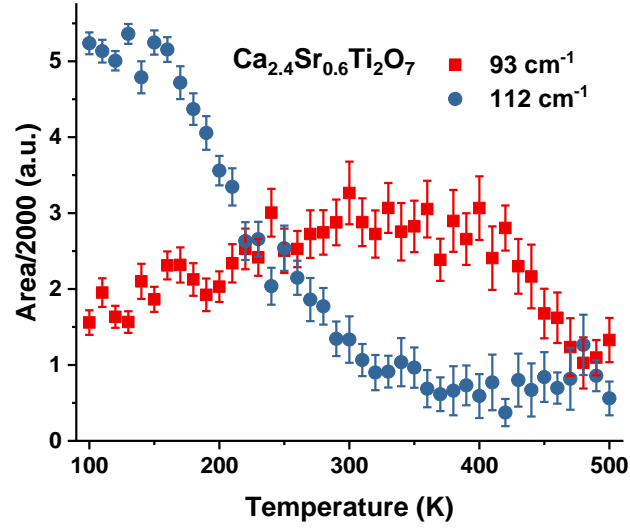
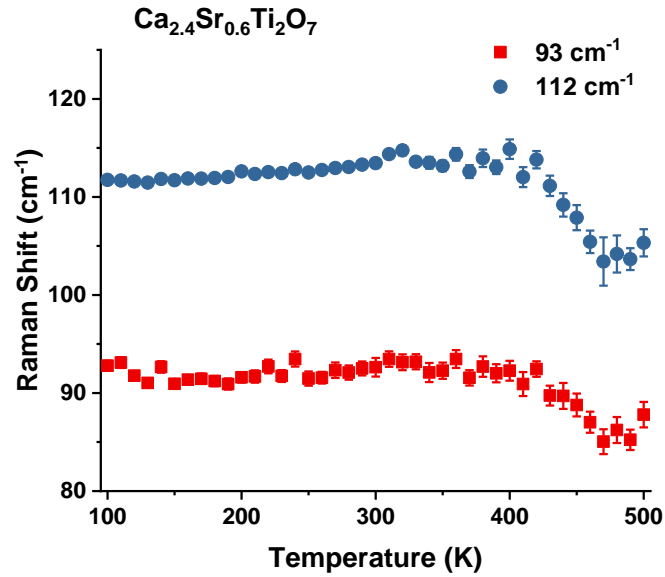


Fig. S7. Raman spectra for $\text{Ca}_{2.4}\text{Sr}_{0.6}\text{Ti}_2\text{O}_7$ single crystal (beam direction with respect to crystal not known). The full spectrum is given in (a). Note the reduction in amplitude of the features near 120 cm^{-1} and 200 cm^{-1} which are expanded in (b). Both peak are suppressed at $\sim 420 \text{ K}$. This behavior is similar to that seen in $\text{Ca}_3\text{Mn}_2\text{O}_7$. Data are from cooling curves.



(a)



(b)

Fig. S8. Extracted parameters for 93 and 112 cm^{-1} peaks for $\text{Ca}_{2.4}\text{Sr}_{0.6}\text{Ti}_2\text{O}_7$ single crystal. Note the decay of the 112 cm^{-1} peaks amplitude by 300 K in (a), and the softening of the 93 and 112 cm^{-1} peaks above 400 K. Data are from cooling curves.

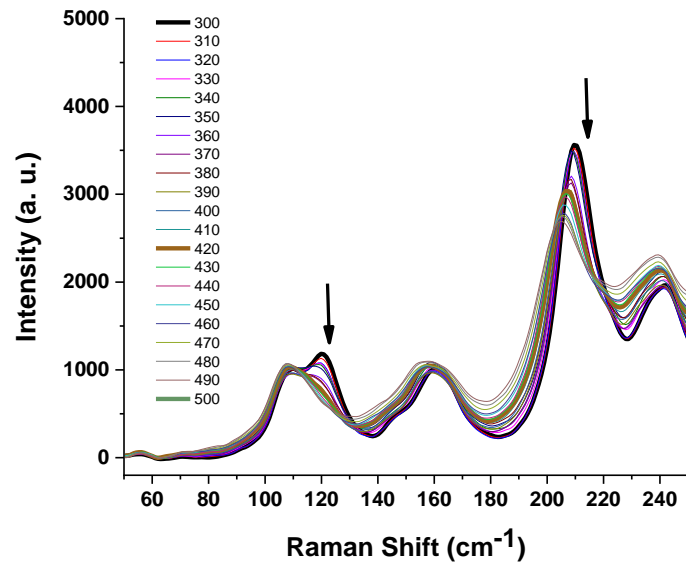


Fig. S9. Raman spectra for $\text{Ca}_3\text{Ti}_2\text{O}_7$ polycrystalline sample. Note the reduction in amplitude of features near 120 cm^{-1} and 200 cm^{-1} have the same behavior as the temperature increases up to $\sim 420 \text{ K}$ (vanish) as the $\text{Ca}_{2.4}\text{Sr}_{0.6}\text{Ti}_2\text{O}_7$ single crystal sample. Hence there is a common type of structural transition near $\sim 400 \text{ K}$ in the Ti and Mn-based systems. Data are from warming curves.

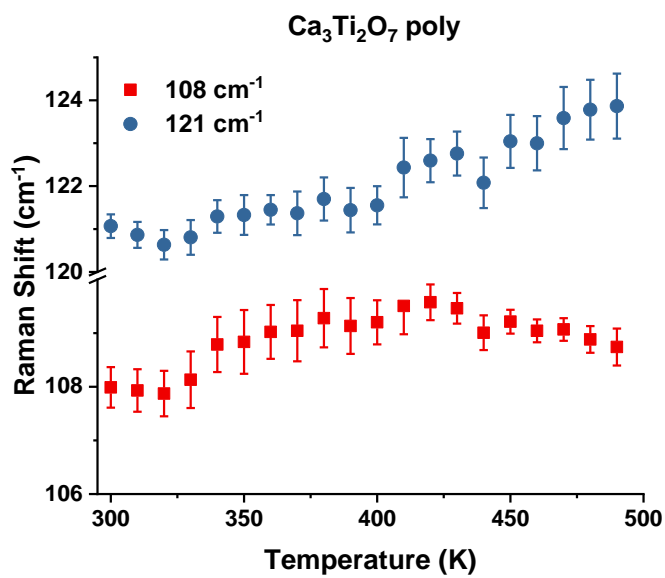
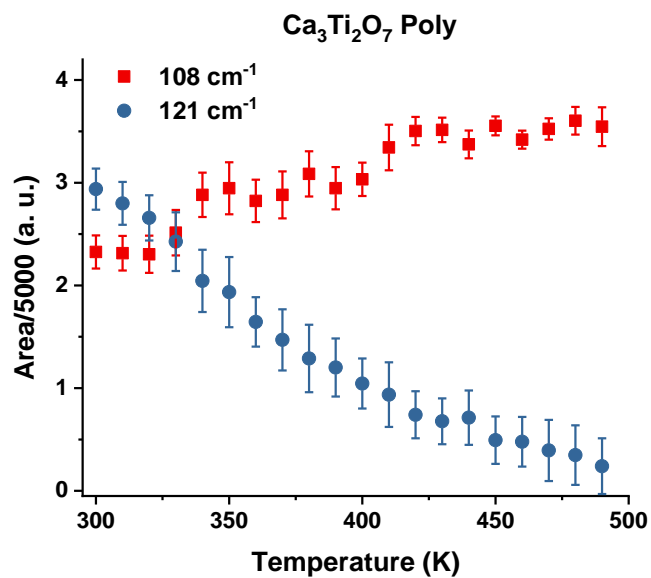


Fig. S10. Extracted parameters for 108 and 121 cm⁻¹ peaks for Ca₃Ti₂O₇ powder sample. Note the decay of the 121 cm⁻¹ peaks amplitude with temperature in (a). The phonon modes harden with increasing temperature. Data are from warming curves.

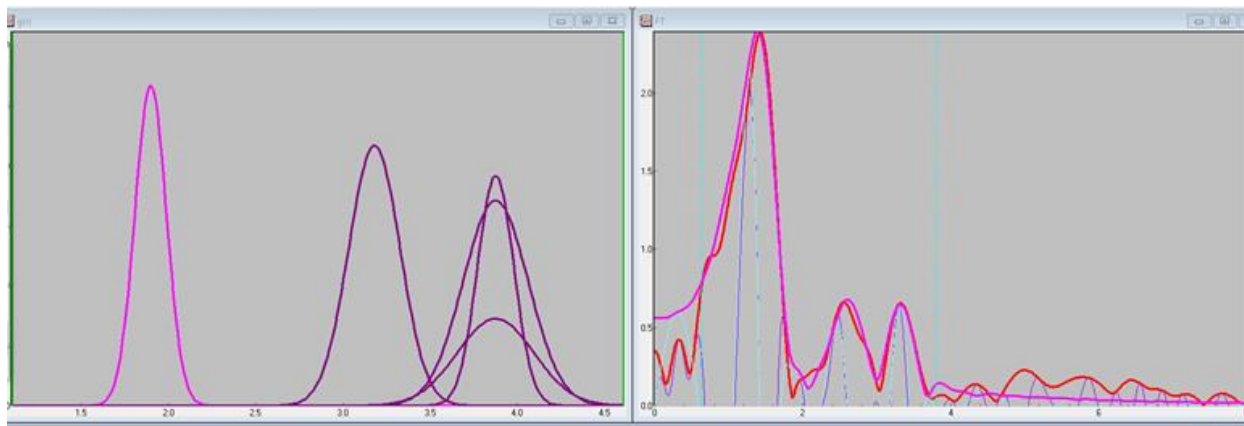


Fig. S11. (Left Panel) Fit to $\text{Ca}_3\text{Mn}_2\text{O}_7$ Mn K-edge data at 880 K showing the single scattering $g(r)$ Gaussian peaks for the Mn-O shell and the Mn-Ca shell and both single and multiple scattering contributions for the nearest neighbor in plane Mn-Mn peak. The full R-space fit over the same three shells also given (Right Panel). The peak near 4.0 Å (left panel) includes multiple scattering contributions.

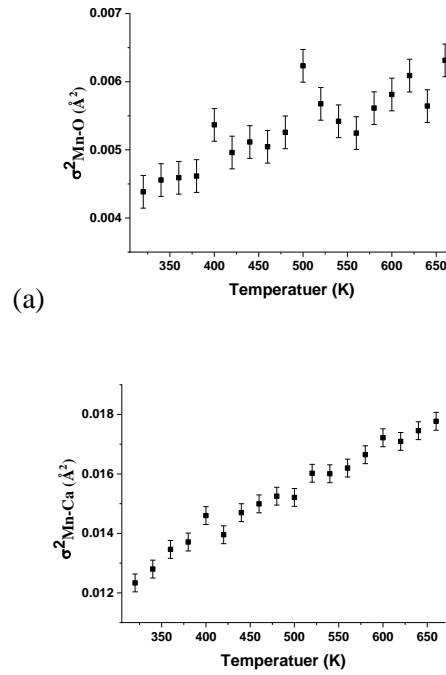


Fig. S12. XAFS structure function of $\text{Ca}_3\text{Mn}_2\text{O}_7$ measured between 320 K and 700 K (in (a) and (b)) revealing that the Mn-O and Mn-Ca Correlations. Note the change in the Mn-O correlation near 400 and 500K.

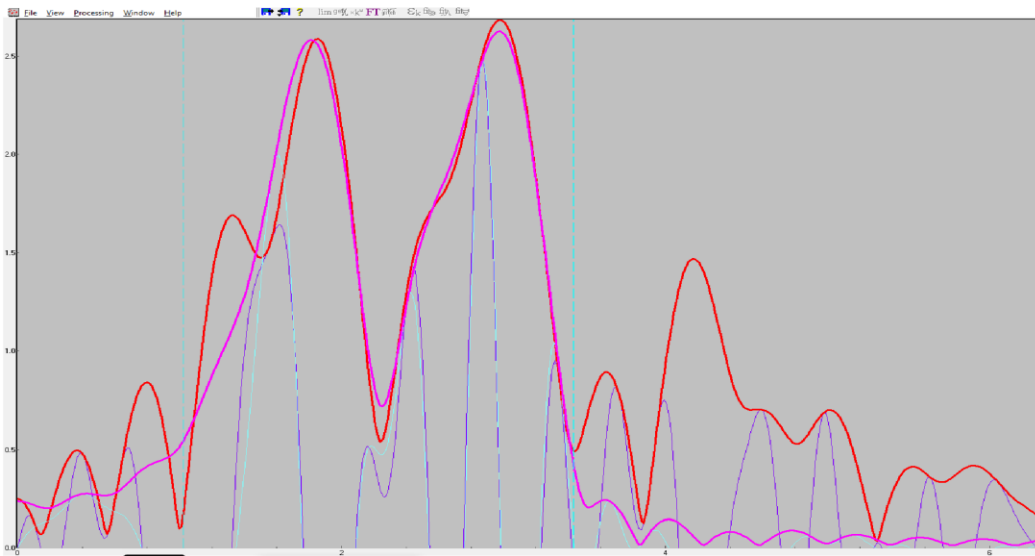
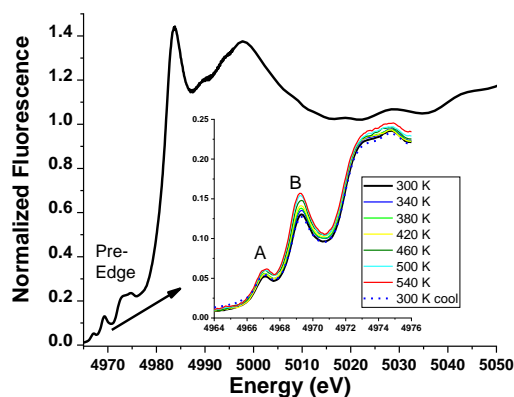


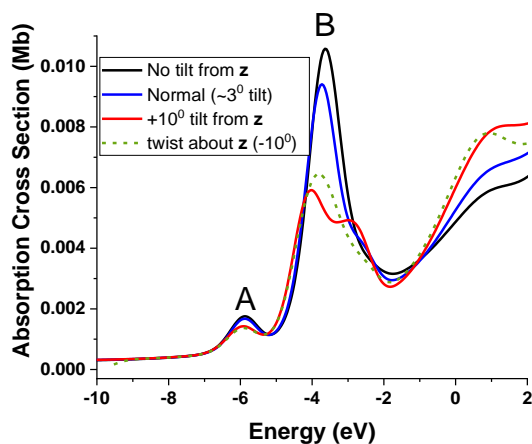
Fig. S13. Fit to Ca K-edge XAFS of $\text{Ca}_3\text{Mn}_2\text{O}_7$ in R-space for data (crystal derived powder) taken at 350 K. Extracted structural parameters are given in Table S2 at multiple temperatures (300, 350 and 450 K).

Table S2. Ca K-Edge XAFS Derived Structural Parameters

Average Bond Distance (Å)		Gaussian Width (Å)
300 K		
Ca-O	2.30(1)	0.007(1)
Ca-Mn	3.13(1)	0.009(1)
Ca-Ca	3.62(1)	0.003(1)
350 K		
Ca-O	2.35(2)	0.008(2)
Ca-Mn	3.15(1)	0.007(1)
Ca-Ca	3.63(2)	0.004(2)
450 K		
Ca-O	2.34(2)	0.011(2)
Ca-Mn	3.17(1)	0.008(2)
Ca-Ca	3.64(2)	0.006(2)



(a)



(b)

Fig. S14. (a) Ti K-edge XANES spectra of $\text{Ca}_{2.4}\text{Sr}_{0.6}\text{Ti}_2\text{O}_7$ between (crystal ground into powder sample) for temperatures between 300 and 540. In the inset, note that the pre-edge peak B intensity increase with increasing temperature. (b) Simulated spectra for a CaTiO_3 cluster for 119 atoms centered on Ti. Note that reduction of tilting relative to the long axis (called x here, Fig. 1(a)) increases the amplitude of peak B while reduction of twisting about the z-axis reduces the peak amplitude (dotted line). Hence the observed continuous enhancement of the B feature with temperature indicates continuous reduction of the tilting of the TiO_6 polyhedra with increasing temperature in $\text{Ca}_{2.4}\text{Sr}_{0.6}\text{Ti}_2\text{O}_7$.

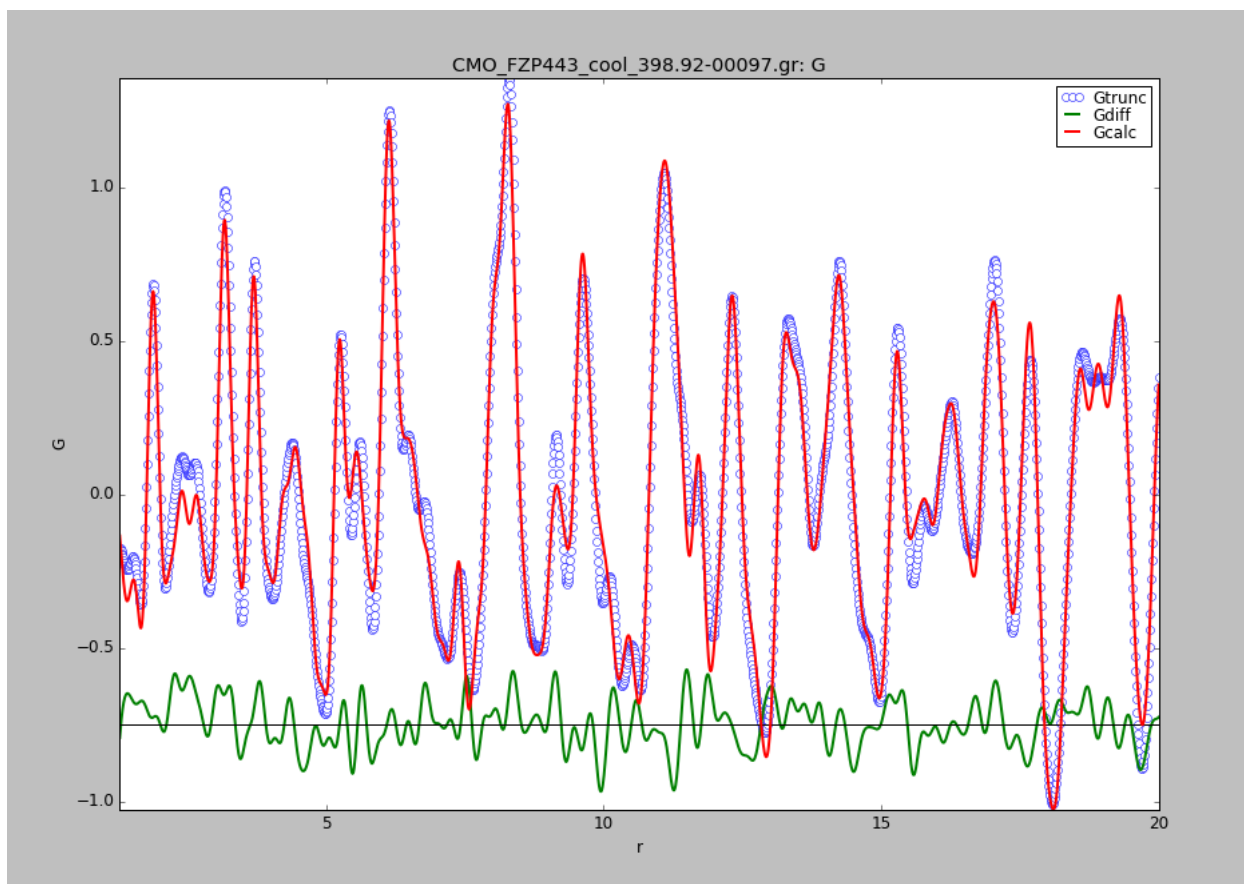
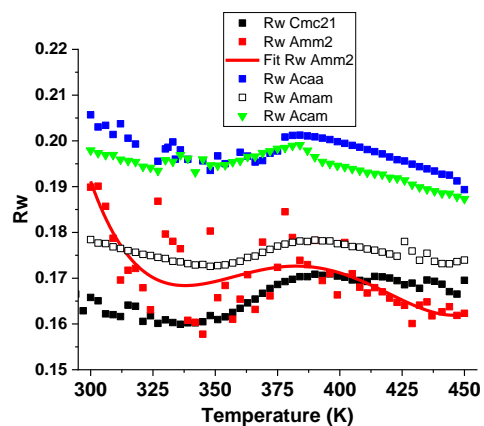
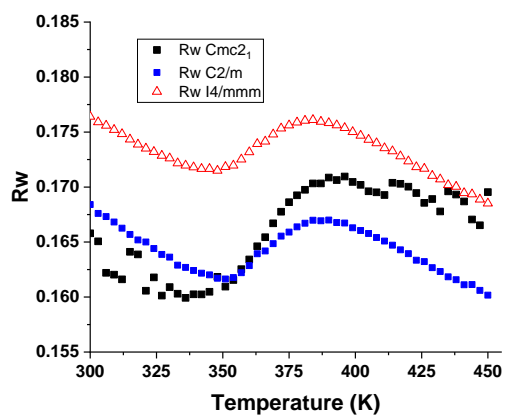


Fig. S15. R-Space PDF fit between 1.3 and 20 Å for the $\text{Cmc}2_1$ model for typical data taken at 399 K. The lower curve is the difference between the model (solid red line) and the data (open circles). Fits were conducted with PDFgui [15].



(a)



(b)

Fig. S16. (a) R_w fitting parameters for $\text{Ca}_3\text{Mn}_2\text{O}_7$ from PDF fits show that the $\text{Cmc}2_1$ space group gives the best model up to ~ 400 K while a possible space group for higher temperatures is the polar $\text{Amm}2$ space group. (b) Utilizing the space group (unit cell) results from single crystal measurements, it is seen that the best model above the first order transition is the $\text{C}2/m$ cell with volume $\frac{1}{2}$ that of the low-temperature $\text{Cmc}2_1$ cell. Data are from cooling curves.

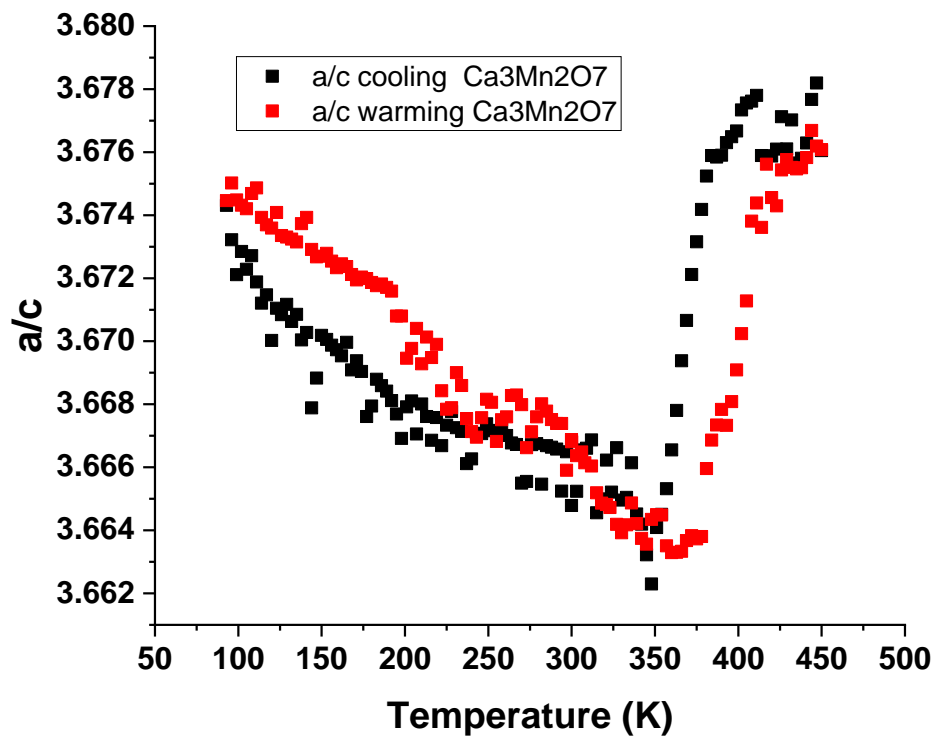
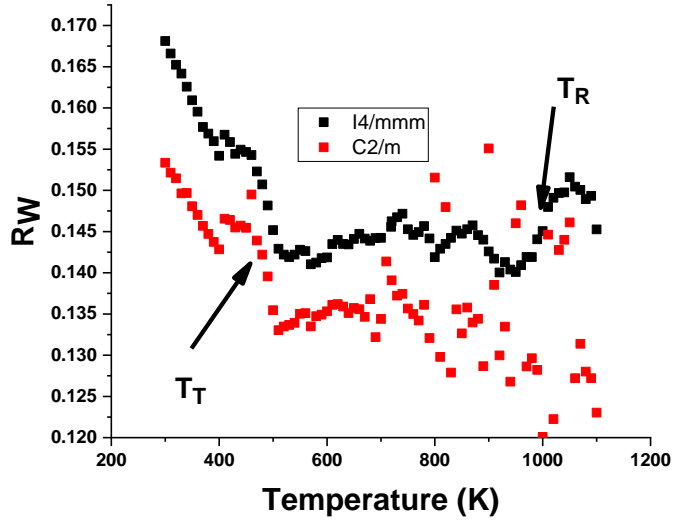


Fig. S17. Ratio of a to c lattice parameter $\text{Ca}_3\text{Mn}_2\text{O}_7$ (based on single crystal sample) during warming and cooling based on PDF fits.

(a)



(b)

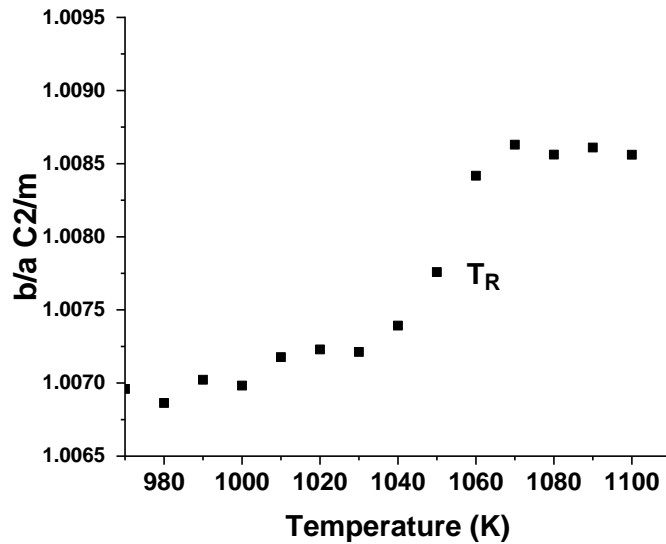


Fig. S18. (a) Fit of the parameter (for single crystal derived $\text{Ca}_3\text{Mn}_2\text{O}_7$ powder) for short range structure PDF data covering same r -range as in Fig. S15 (1.3 to 20 Å). The local structure is consistent with the $C2/m$ space group for the full temperature range. (a) b/a ratio ($C2/m$ space group) near the high-temperature transition at ~ 1050 K. Measurements were made on warming.

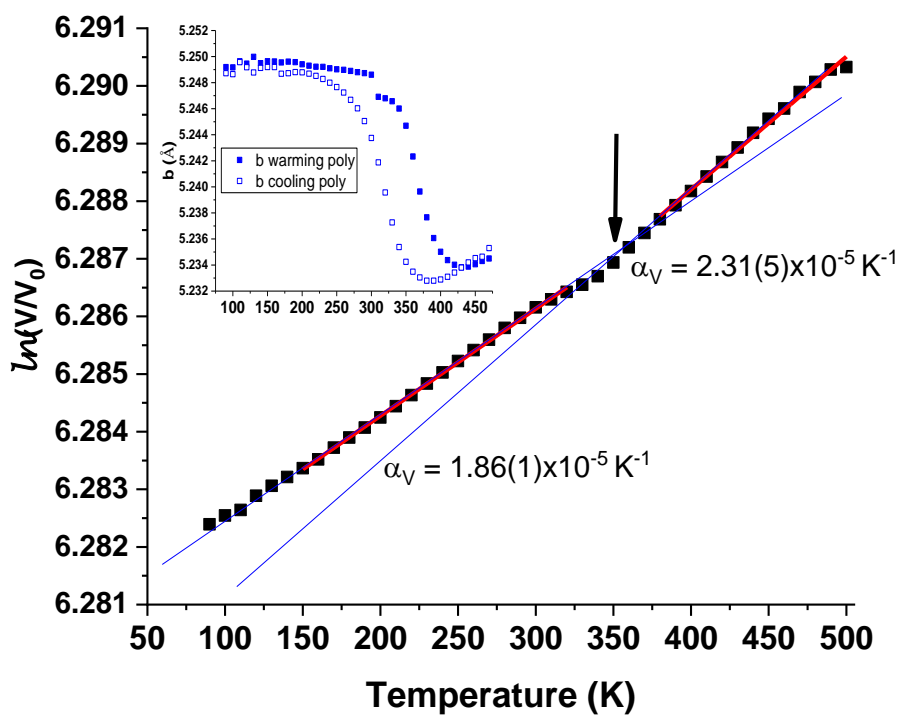


Fig. S19. Volume and b lattice parameter vs. temperature for polycrystalline $\text{Ca}_3\text{Ti}_2\text{O}_7$. Note broad range of separation for the b parameter (inset) for warming and cooling. The broad hysteresis is due to defects in powder prepared samples. Data in the main figure are from PDF cooling curves.

Table S3. Structural Parameters from Single Crystal Solution for Ca₃Mn₂O₇ at 480 K (I4/mmm)

Atoms	x	y	z	Ueq (Å ²)×10 ³		
Mn	5000	5000	4018.7(6)	6.6(4)		
Ca1	5000	5000	1865.3(9)	13.3(5)		
Ca2	0	0	5000	13.7(6)		
O1 (apical interior)	5000	5000	5000	20.0(16)		
O2 (apical)	5000	5000	3040(3)	14.3(10)		
O3 (in-plane)*	4188(12)	0	4031(2)	14.2(11)		
Atom	U ₁₁ (Å ²)×10 ³	U ₂₂ (Å ²)×10 ³	U ₃₃ (Å ²)×10 ³	U ₁₂ (Å ²)×10 ³	U ₁₃ (Å ²)×10 ³	U ₂₃ (Å ²)×10 ³
Mn	6.0(5)	6.0(5)	7.7(6)	0	0	0
Ca1	14.5(6)	14.5(6)	10.7(8)	0	0	0
Ca2	13.2(7)	13.2(7)	14.6(10)	0	0	0
O1	28(2)	28(2)	3(2)	0	0	0
O2	17.0(14)	17.0(14)	8.9(16)	0	0	0
O3	12(2)	6.8(18)	24(2)	0	-4.3(13)	0

Space Group: I4/mmm (Z=2) Tetragonal Cell
a = 3.7054 (3) Å, c = 19.585 (3) Å, Dx = 4.225 g/cm³

Measurement Temperature: 480 K

Crystal Dimensions: ~20 μm (diameter)

Wavelength: 0.41328 Å,

Absorption Coefficient: 1.783 mm⁻¹

F(000) = 333.4

Reflections Collected: 5325

2θ Range : 2.42° to 40.2°

-6 ≤ h ≤ 6, -6 ≤ k ≤ 5, and -31 ≤ l ≤ 32,

Number of Measured Reflections: 5325

Number of Independent Reflections: 241

Number of fitting parameters: 20

Restraints = 0

Max and Min Peak in Final Difference Map: 3.1/-1.0 e-/ Å³

R₁ = 4.42 %, wR₂ = 18.8 %, Goodness of Fit = 1.63 (I ≥ 2σ (I))

R₁ = 4.56 %, wR₂ = 19.0 % (all data)

$$R_1 = \frac{\sum ||F_0| - |F_c||}{\sum |F_0|}$$

$$wR_2 = \frac{\sum w(F_o^2 - F_c^2)^2}{\sum w(F_o^2)^2}$$

* O3 atoms have 50% occupancy of two sites.

**Table S4. Bond Distances
in Ca₃Mn₂O₇ at 480 K**

Atoms	Distance (Å)
Mn-O3	1.8771(7) x 4
Mn-O2	1.922(1)
Mn-O2	1.916(6)
Ca1-O2	2.301(6)
Ca1-O3	2.344(4) x 2
Ca1-O2	2.6266(5) x 4
Ca1-O2	2.779(5) x 2
Ca2-O3	2.451(4) x 4
Ca2-O2	2.6201(4) x 4
Ca2-O3	2.870(4) x 4
Mn-Ca1	3.1405(9) x 4
Mn-Ca2	3.2494(7) x 4
$\langle R_{\text{Mn-O}} \rangle = 1.89 \text{ \AA}$, Standard Dev = 0.02 Å	
$\langle R_{\text{Ca-O}} \rangle = 2.61 \text{ \AA}$, Standard Dev = 0.18 Å	
$\langle R_{\text{Mn-Ca}} \rangle = 3.19 \text{ \AA}$, Standard Dev = 0.05 Å	

Table S5. Structural Parameters from Single Crystal Solution for Ca₃Mn₂O₇ at 480 K (C2/m low symmetry solution)

Atoms	x	y	z	Ueq (Å ²)×10 ³		
Mn	5983.5(10)	5000	8035.1(8)	7.1(3)		
Ca1	8135.4(19)	5000	3731.0(12)	14.1(3)		
Ca2	5000	0	10000	14.4(4)		
O1 (apical interior)	5000	5000	10000	21.5(11)		
O2 (apical)	6960(6)	5000	6081(4)	14.0(7)		
O3	3870(16)	2103(17)	8060(6)	15.2(16)		
O3P	3052(18)	2917(17)	8064(7)	14.6(16)		
Atom	U ₁₁ (Å ²)×10 ³	U ₂₂ (Å ²)×10 ³	U ₃₃ (Å ²)×10 ³	U ₁₂ (Å ²)×10 ³	U ₁₃ (Å ²)×10 ³	U ₂₃ (Å ²)×10 ³
Mn	6.6(4)	6.7(4)	8.2(4)	-0	-2.2(3)	0
Ca1	15.1(5)	15.5(6)	11.7(5)	-0	-3.6(4)	0
Ca2	13.3(6)	14.5(7)	15.4(7)	-0	-3.6(5)	0
O1	27(3)	31(3)	5.9(18)	-0	-3.5(19)	0
O2	12.4(14)	20.5(17)	7.8(12)	-0	-0.1(10)	0
O3*	11(3)	13(3)	21(2)	-1(2)	-3.5(19)	-4.3(19)
O3P	12(3)	10(3)	25(3)	-3(2)	-10(2)	2(2)

Space Group: C2/m (Z=2) Monoclinic Cell
a = 5.2404(7) Å, 5.2401(7) Å, c = 10.1369(14) Å, Dx = 4.225 g/cm³
b = 75.024(3)°
Measurement Temperature: 480 K
Crystal Dimensions: ~20 μm (diameter)
Wavelength: 0.41328 Å,
Absorption Coefficient: 1.783 mm⁻¹
F(000) = 333.4
Reflections Collected: 5325
2θ Range : 2.42° to 40.2°
-8 ≤ h ≤ 8, -8 ≤ k ≤ 7, and -16 ≤ l ≤ 16
Number of Measured Reflections: 5325
Number of Independent Reflections: 687
Number of fitting parameters: 46
Restraints = 0
Max and Min Peak in Final Difference Map: 3.1/-1.7 e-/Å³
R₁ = 4.77 %, wR₂ = 15.5 %, Goodness of Fit = 1.53 (I ≥ 2σ (I))
R₁ = 5.60 %, wR₂ = 19.7 % (all data)

$$R_1 = \frac{\sum ||F_o| - |F_c||}{\sum |F_o|}$$

$$wR_2 = \frac{\sum w(F_o^2 - F_c^2)^2}{\sum w(F_o^2)^2}$$

* O3 and O3P atoms have 50% occupancy of the two sites (derived from fit).

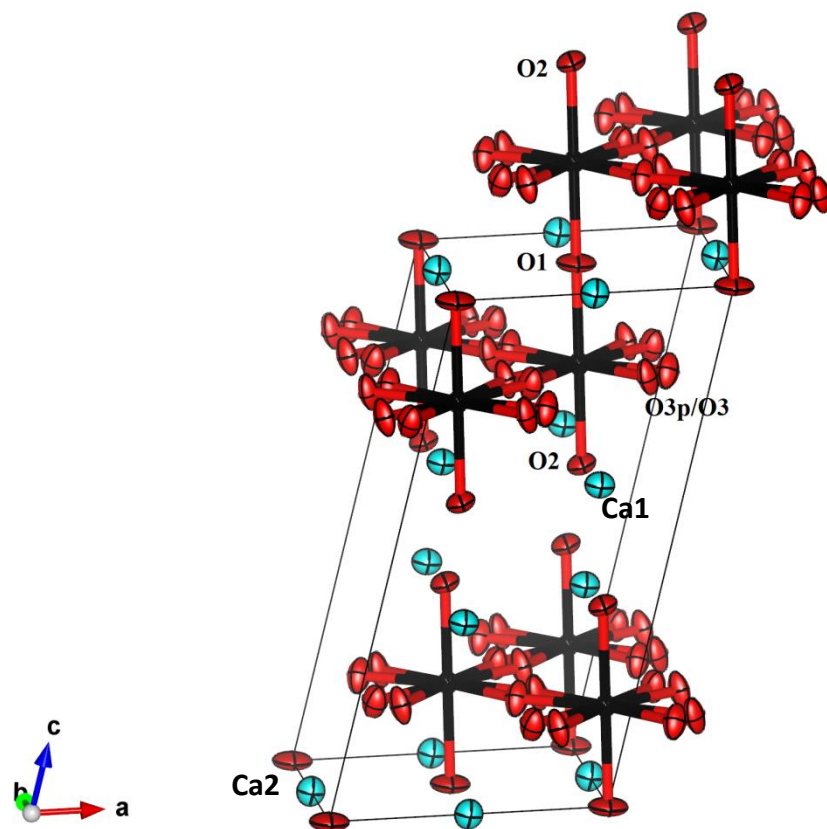


Fig. S20. Unit cell for the low symmetry solution ($C2/m$) to 480 K data for $\text{Ca}_3\text{Mn}_2\text{O}_7$. Note (as in $I4/mmm$ solution) that there is a 50/50 split occupancy at the O3 site in-plane due to domain formation.

Table S6. Structural Parameters from Single Crystal Solution of Ca₃Mn₂O₇ at 300 K

Atoms	x	y	z	Ueq (Å ²)×10 ³		
Mn	-4018.5(5)	-7504.8(13)	-2684.3(19)	5.8(2)		
Ca1	-3136.9(7)	-7453(2)	-7846(2)	9.5(3)		
Ca2	5000	-2507(4)	-2487(3)	10.9(4)		
O1	5000	-7948(11)	-2709(14)	12.5(12)		
O2	-3040(2)	-7208(8)	-2627(10)	9.5(8)		
O3	-4112(2)	-4623(6)	-4780(10)	11.2(7)		
O4	-3943.2(19)	-9641(7)	-5515(11)	12.0(7)		
Atom	U11(Å ²)×10 ³	U22(Å ²)×10 ³	U33(Å ²)×10 ³	U12(Å ²)×10 ³	U13(Å ²)×10 ³	U23(Å ²)×10 ³
Mn	6.2(4)	7.0(4)	4.1(4)	0.05(15)	1.6(3)	-0.19(16)
Ca1	8.5(5)	12.2(5)	7.7(6)	-0.5(3)	0.3(5)	1.2(3)
Ca2	10.6(7)	12.3(6)	9.7(9)	-0	-0	-2.1(5)
O1	4.8(18)	16(3)	17(3)	-0	-0	-2(3)
O2	7.2(13)	9.9(15)	11(2)	-0.9(10)	-2(2)	0.1(15)
O3	15.1(15)	8.1(16)	10.3(15)	-1.1(12)	0.1(13)	0.9(13)
O4	15.4(14)	8.9(15)	11.6(17)	-0.6(11)	0.7(14)	-3.0(16)

Space Group: Cmc2₁ (Z=4) Orthorhombic Cell

a = 19.4387(12) Å, b = 5.2493(3) Å, c = 5.2433(3) Å, Dx = 4.247 g/cm³

Measurement Temperature: 300 K

Crystal Dimensions: ~20 μm (diameter)

Wavelength: 0.41328 Å,

Absorption Coefficient: 1.792 mm⁻¹

F(000) = 666.8

Reflections Collected: 10565

2θ Range : 2.44° to 40.3°

-32 ≤ h ≤ 32, -7 ≤ k ≤ 8, and -8 ≤ l ≤ 8

Number of Measured Reflections: 10,565

Number of Independent Reflections: 1296

Number of fitting parameters: 58

Restraints = 1

Flack Parameter = 0.4(3)

Max and Min Peak in Final Difference Map: 3.2/-2.7 e-/Å³

R₁ = 5.23 %, wR₂ = 14.7 %, Goodness of Fit = 1.54 (I ≥ 2σ (I))

R₁ = 7.15 %, wR₂ = 21.3 % (all data)

$$R_1 = \frac{\sum ||F_0| - |F_c||}{\sum |F_0|}$$

$$wR_2 = \frac{\sum w(F_o^2 - F_c^2)^2}{\sum w(F_o^2)^2}$$

**Table S7. Bond Distances
in Ca₃Mn₂O₇ at 300 K**

Atoms	Distance (Å)
Mn-O1	1.9221(12)
Mn-O2	1.908(4)
Mn-O3	1.897(5)
Mn-O3	1.879(4)
Mn-O4	1.887(5)
Mn-O4	1.866(5)
Ca1-O2	2.298(4)
Ca1-O2	2.457(4)
Ca1-O2	2.517(6)
Ca1-O2	2.811(4)
Ca1-O2	2.457(4)
Ca1-O2	2.457(4)
Ca1-O3	2.895(5)
Ca1-O3	2.410(4)
Ca1-O4	2.295(5)
Ca1-O4	2.597(5)
Ca2-O1	2.748(8)
Ca2-O1	2.517(8)
Ca2-O1	2.859(5)
Ca2-O1	2.396(5)
Ca2-O3	2.379(5)
Ca2-O3	2.696(5)
Ca2-O3	2.379(5)
Ca2-O3	2.696(5)
Ca2-O4	2.561(4) x 2
Mn-Ca1	3.0617(15)
Mn-Ca1	3.1171(14)
Mn-Ca1	3.1543(13)
Mn-Ca1	3.2032(12)
Mn-Ca2	3.2457(18)
Mn-Ca2	3.2473(18)
Mn-Ca2	3.1596(19)
Mn-Ca2	3.3264(18)

$\langle R_{\text{Mn-O}} \rangle = 1.89 \text{ \AA}$, Standard Dev = 0.02 Å

$\langle R_{\text{Ca-O}} \rangle = 2.55 \text{ \AA}$, Standard Dev = 0.18 Å

$\langle R_{\text{Mn-Ca}} \rangle = 3.19 \text{ \AA}$, Standard Dev = 0.08 Å

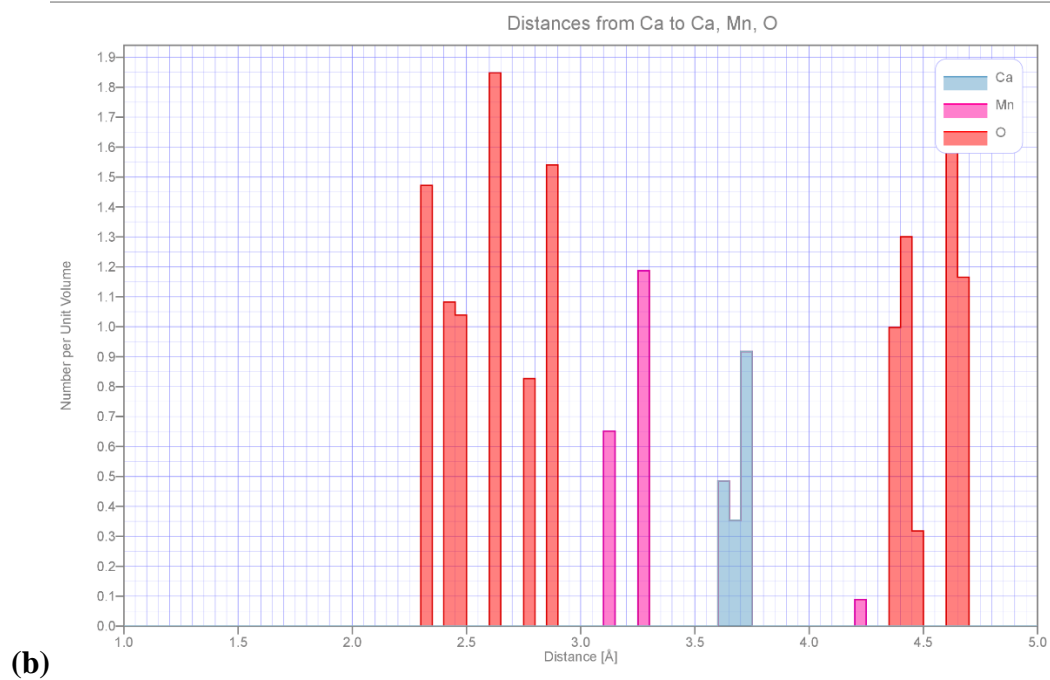
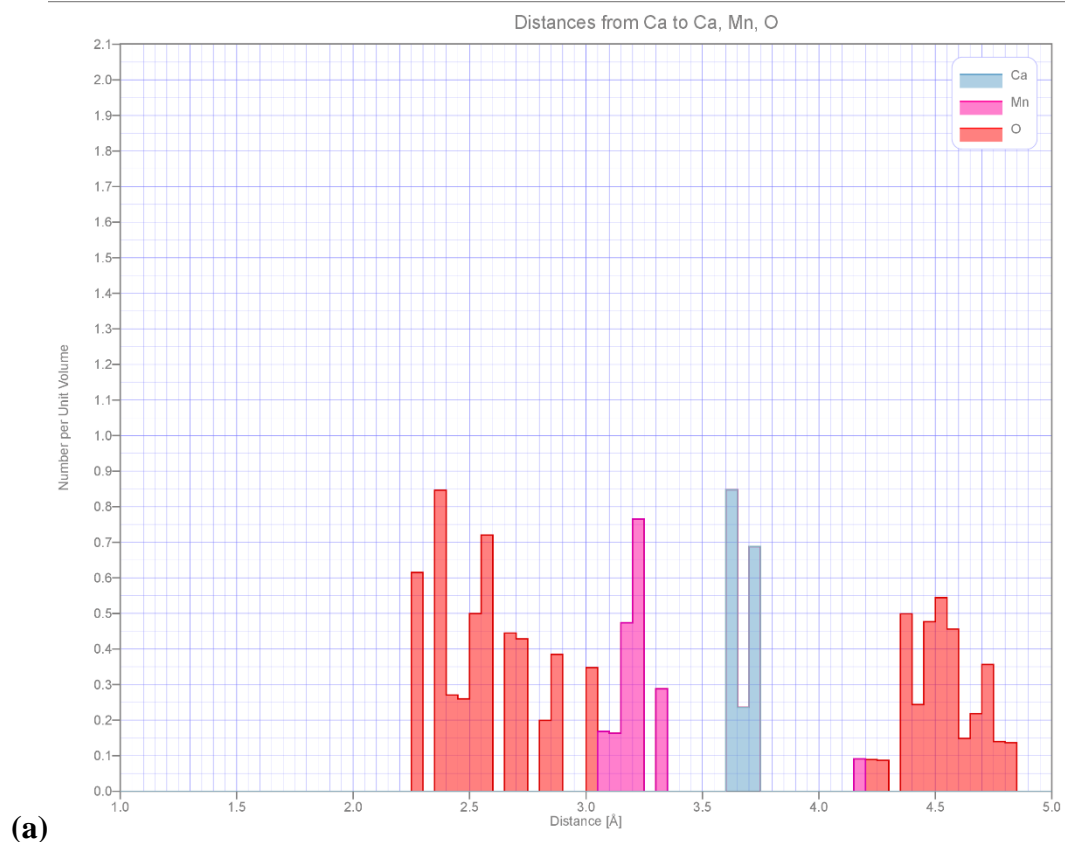


Fig. S21. Distribution of atoms about Ca at 300 K (a) and at 480 K (b) taken from the single crystal structure solution. Note the strong sharpening of the Ca-Mn distribution (pink blocks) at high temperature.

References

-
- [1] (a) Y. S. Oh, X. Luo, F.-T. Huang, Y. Wang, and S.-W. Cheong, *Nature Materials* **14**, 407 (2015).
(b) B. Gao, F.-T. Huang, Y. Wang, J.-W. Kim, Y. Wang, S.-J. Lim, and S.-W. Cheong, *Appl. Phys. Lett.* **110**, 222906 (2017).
- [2] (a) A. Dewaele A., M Torrent, P. Loubeyre and M. Mezouar *Phys. Rev. B* **78**, 104102 (2008).
(b) H. K. Mao, J. Xu, and P. M. Bel, *J. Geophys. Res.* **91**, 4673 (1986).
(c) <http://millenia.cars.aps.anl.gov/gsecars/ruby/ruby.htm>
- [3] Y. Akahama and H. Kawamura, *J. Appl. Phys.* **100**, 043516 (2006).
- [4] O. V. Dolomanov, L. J. Bourhis, R. J. Gildea, J. A. C. Howard, and H. Puschmann, *J. Appl. Cryst.* **42**, 339 (2009).
- [5] G. Kresse and D. Joubert, *Phys. Rev. B* **59**, 1758 (1999).
- [6] C. J. Fennie and K. M Rabe, *Phys. Rev. B* **72**, 100103(R) (2005).
- [7] L.-F. Huang, X.-Z. Lu and J. M. Rondinelli, *Phys. Rev. Lett.* **117**, 1159011 (2016).
- [8] Atsushi Togo and Isao Tanaka, *Scr. Mater.*, **108**, 1-5 (2015)
- [9] (a) T. A. Tyson, M. Deleon, S. Yoong, and S. W. Cheong, *Phys. Rev. B: Condensed Matter and Materials Physics* **75**, 174413 (2007).
(b) B. Ravel and M. Newville, *J. Synchrotron Rad.* **12**, 537 (2005); *X-Ray Absorption: Principles, Applications, Techniques of EXAFS, SEXAFS and XANES*, edited by D. C. Konningsberger and R. Prins (Wiley, New York, 1988).
- [10] K.V. Klementev, *J. Phys. D* **34**, 209 (2001).
- [11] T. A. Tyson, M. Deleon, S. Yoong, and S. W. Cheong, *Physical Review B* **75**, 174413 (2007).
- [12] Q. Qian, T. A. Tyson, C.-C.Kao, M. Croft, S.-W. Cheong, and , M. Greenblatt, *Rev. B* **64**, 22430 (2001).
- [13] (a) T. A. Tyson, (unpublished). (b) T. A. Tyson, *Phys. Rev.* **49**, 12578 (1994).

[14] (a) R. B. Neder and Th. Proffen, *Diffuse Scattering and Defect Structure Simulations*, (Oxford University, Oxford, 2008).

(b) T. Egami and S. L. J. Billinge, *Underneath the Bragg Peaks: Structural Analysis of Complex Materials*, (Pergamon, Amsterdam, 2003).

(c) Th. Proffen, S. J. L. Billinge, T. Egami and D. Louca, *Z. Kristallogr* **218**, 132 (2003).

(d) V. Petkov, in *Characterization of Materials*, (John Wiley and Sons, Hoboken, 2012).

[15] P. Juhás, C. L. Farrow, X. Yang, K. R. Knox and S. J. L. Billinge, *Acta Crystallogr. A* **71**, 562 (2015)